Systematic search of $\pi h_{11/2} \otimes \nu h_{11/2}$ chiral doublet bands and role of triaxiality in odd-odd $Z=55$ isotopes: ^{128,130,132,134}Cs

T. Koike, K. Starosta, C. J. Chiara,* D. B. Fossan, and D. R. LaFosse
Department of Physics and Astronomy, State University of New York at Stony Brook, Stony Brook, New York 11794-3800
(Received 22 October 2002; published 30 April 2003)

The odd-odd Cs isotopes $^{128-134}$Cs have been investigated in search of chiral doublet bands. Two nearly degenerate bands built on the $\pi h_{11/2} \otimes \nu h_{11/2}$ configuration have been identified in $^{128-132}$Cs. Systematics of various experimental observables associated with the partner bands are presented. The $B(M1)_{In}/B(M1)_{Out}$ staggering with spin was discovered to be in phase with the $B(M1)/B(E2)$ staggering for the yrast partner band. A core-quasiparticle coupling model employing the Kerman-Klein-Dönau-Frauendorf method was applied to study ^{128}Cs. A triaxial core with an irrotational-flow moment of inertia was assumed. The chiral features, as well as previously known experimental characteristics of the $\pi h_{11/2} \otimes \nu h_{11/2}$ yrast partner band, are well reproduced demonstrating the important role played by triaxiality in the underlying physics in these nuclei.

DOI: 10.1103/PhysRevC.67.0343XX PACS number(s): 27.60.+j, 21.60.−n, 23.20.Lv, 21.10.Re

I. INTRODUCTION

The complexity of odd-odd nuclei has been a difficult challenge for both experimental and theoretical nuclear studies. Yet relatively simple nuclear structures emerge at high spin involving a wealth of physical phenomena, from which the delicate interplay between collective and single-particle degrees of freedom can be investigated. One such study involves the observation of chirality in odd-odd $N=75$ and 73 isotones in the $A\sim130$ region [1–5]. The common experimental characteristics of chirality that were observed in these nuclei are the nearly degenerate doublet $\Delta I=1$ rotational bands built from the $\pi h_{11/2} \otimes \nu h_{11/2}$ configuration.

Experiments and calculations indicate that even-even transitional nuclei in this mass region have triaxial deformations that are soft relative to the triaxial parameter γ. The Fermi level of these even-even nuclei lies in the lower proton $h_{11/2}$ subshell and in the upper neutron $h_{11/2}$ subshell. When an $h_{11/2}$ proton, prolate driving, is added to an even-even γ-soft core, it will align its single-particle angular momentum $\mathbf{j}_\pi$ with the short axis to minimize energy. On the other hand, when an $h_{11/2}$ neutron hole, oblate driving, is added to the core, its angular momentum $\mathbf{j}_\nu$ will orient along the long axis. Therefore, when both a proton and a neutron from opposite-shape-driving orbits are added to a γ-soft core, it is expected that the resulting equilibrium shape of the odd-odd nucleus will have a relatively stable triaxial shape. With the rotational invariance of the system broken by the deformed shape in the intrinsic frame, rotational bands result from this collective degree of freedom, whose properties can be studied in terms of a quantum mechanical triaxial rotor characterized solely by the moment of inertia of the core plus the valence particles. This moment of inertia, which can be modeled by irrotational flow, is largest along the intermediate axis for triaxial shapes. As a result, the collective rotation $\mathbf{R}$ is oriented along this axis.

The above scenario leads to three mutually orthogonal angular momenta, namely, $\mathbf{j}_\pi$, $\mathbf{j}_\nu$, and $\mathbf{R}$, resulting in a chiral geometry. The most notable consequence of chirality is a doubling of the rotational states. In particular, two nearly degenerate $\Delta I=1$ bands built from the $\pi h_{11/2} \otimes \nu h_{11/2}$ configuration in $A\sim130$ odd-odd nuclei are expected because of the favorable conditions for the formation of a chiral geometry. A well developed sideband associated with the yrast band in ^{134}Pr [6] was observed before the chiral interpretation was proposed by Frauendorf and Meng [7]. States with spin I in the sideband lie $\sim$300 keV above those with the same spin in the yrast band near $I=(10)^+$, but as the spin increases the related states with the same I become closer in their energy achieving near degeneracy at (14^+) and (15^+)[1] with a separation of $\sim$50 keV [6]. Since there is no *a priori* reason to consider ^{134}Pr as a special nucleus of this region in terms of the underlying physics, the present work was designed to search for chiral doublet bands in the nearby odd-odd $^{128-134}$Cs isotopes. In reporting these results for $^{128-134}$Cs, this paper will focus on the positive-parity bands in odd-odd Cs isotopes and their systematic properties. Brief results for ^{128}Cs and ^{130}Cs have been presented in Refs. [3,1], respectively, as a part of $N=73$ and $N=75$ systematics studies.

The $\pi h_{11/2} \otimes \nu h_{11/2}$ configuration is comprised of two unique-parity high-j single-particle orbitals for the region between the $Z,N=50$ and 82 shell gaps. Therefore, this configuration is effectively free from admixing with nearby normal positive-parity $d_{5/2}$ and $g_{7/2}$ orbitals. The purity of the configuration greatly facilitates comparisons between experiment and model calculations. Moreover, the yrast $\pi h_{11/2} \otimes \nu h_{11/2}$ bands in odd-odd Cs isotopes have previously drawn considerable attention both experimentally and theoretically. They exhibit systematic properties such as a peculiar spin dependence of the observable $S(I)=[E(I)$

*Present address: Department of Chemistry, Washington University, St. Louis, Missouri 63130.

[1]Based on spin assignments from Ref. [6] which are lower by $1\hbar$ than those proposed in Refs. [1,8].

TABLE I. The reactions, beams, and targets used in the present studies.

Nucleus	Reaction	E_{beam} (MeV)	Pulsed	Target (mg/cm^2)	Pb backing (mg/cm^2)
^{128}Cs	^{122}Sn(^{10}B,4n)	47	Yes	3.0	34
^{130}Cs	^{124}Sn(^{10}B,4n)	47	Yes	3.0	15
^{132}Cs	^{130}Te(^{6}Li,4n)	38	Yes	2.3	10
^{134}Cs	^{130}Te(^{7}Li,3n)	28, 33	No 50	3.0	2

$-E(I-1)]/2I$; this phenomenon, discussed in detail in Sec. IV A 3, is often referred to as *signature inversion*. In addition, $B(M1)/B(E2)$ staggering is observed experimentally. Both systematic properties, however, have eluded definitive theoretical interpretation. Therefore, in Sec. IV A, the observed systematic properties associated with the $\pi h_{11/2} \otimes \nu h_{11/2}$ doublet bands are summarized and accompanied by a discussion of the interpretations. Furthermore, the current study establishes experimentally that a new systematic feature, namely, $B(M1)_{In}/B(M1)_{Out}$ staggering, exists and is in phase with the $B(M1)/B(E2)$ staggering in the yrast band.

The existence of chiral geometries in specific regions provides a clear, but rare window through which physical properties rooted in triaxial nuclear shapes can be observed. For the odd-odd Cs isotopes, the onset of chirality at $N\sim 73$ is a vivid manifestation of the triaxial core as the Fermi level rises in the neutron $h_{11/2}$ subshell with increasing neutron number. The signature inversion and the $B(M1)/B(E2)$ spin dependence, which characterize lighter Cs isotopes, are present as well in the chiral Cs isotopes. This experimental observation suggests that these persistent systematic trends along with chirality can be discussed in terms of common triaxial shape properties and the changing Fermi level in the neutron $h_{11/2}$ subshell. To this end, as a first attempt, a core-quasiparticle coupling model is applied to ^{128}Cs; a slightly different variation of this model was successfully applied to ^{132}La [9] to quantitatively address chiral properties. The details of the theoretical approach are described in Sec. V A. A rigid triaxial rotor with an irrotational-flow moment of inertia is used for the core whose rotational energy and variable moment of inertia are fitted by even-even ^{128}Xe properties. The results show that indeed triaxiality plays a major role in not only predicting the existence of the doublet bands, but also in reproducing reasonably well the staggering phase and magnitude for both the $S(I)$ and the $B(M1)/B(E2)$ ratios. Also, the calculated spin dependence of $B(M1)_{In}/B(M1)_{Out}$ is in agreement with experiment.

On the other hand, the present model is a phenomenological one. The microscopic origin of triaxiality can be revealed by self-consistent calculations. In fact, three-dimensional tilted axis cranking (3D-TAC) calculations have shown substantial triaxiality with a chiral geometry in $N=75$ isotones [1,10]. A systematic theoretical study in the odd-odd Cs iso-

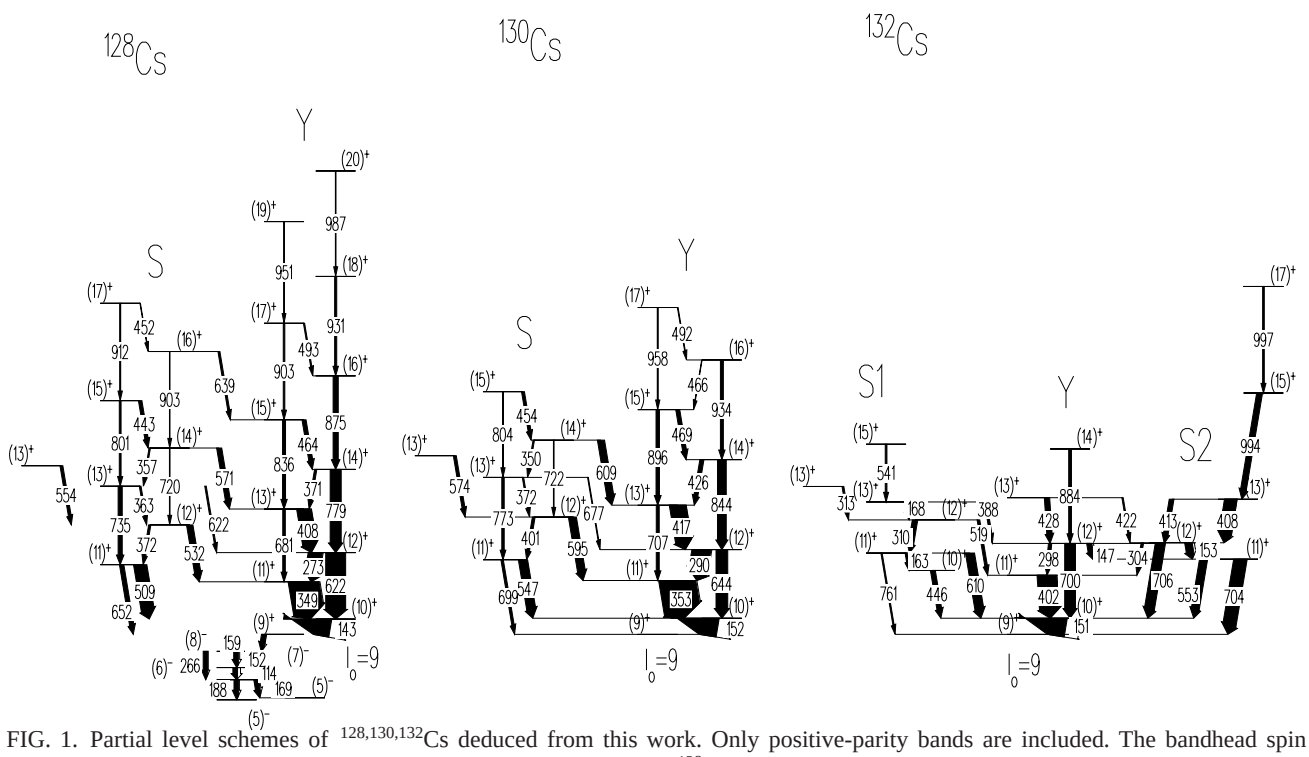

FIG. 1. Partial level schemes of ^{128,130,132}Cs deduced from this work. Only positive-parity bands are included. The bandhead spin is denoted as I_0. As discussed in the text, $I_0=9$ will be supported. For ^{128}Cs, transitions below the isomer, which is indicated by a thick horizontal line, are shown as well.

topes based on relativistic-mean-field tilted axis cranking is underway [11].

II. EXPERIMENTAL METHODS

Excited states in ^{128,130,132,134}Cs have been populated via the ^{122}Sn(^{10}B, $4n$) fusion-evaporation reaction at 47 MeV, ^{124}Sn(^{10}B, $4n$) at 47 MeV, ^{130}Te(^{6}Li, $4n$) at 38 MeV, and ^{130}Te(^{7}Li, $3n$) at 28 MeV and 33 MeV, respectively. Excitation function measurements were carried out for these reactions to determine the beam energies for optimal population strengths. Pulsed beams with a period of 106 ns, provided by the tandem-injected superconducting LINAC at Stony Brook, allowed prompt and delayed timing. In the ^{134}Cs experiment, a continuous dc beam provided by the tandem only was used. Because of a lack of high-spin information, ^{134}Cs was studied with two beam energies; a beam of 28 MeV was chosen to optimize the $3n$ channel, and a higher energy of 33 MeV was used to populate higher-spin states in ^{134}Cs at the expense of an increased $4n$ channel population leading to ^{133}Cs.

An array of six Compton-suppressed HPGe detectors, which were positioned approximately at $\pm 30°$, $\pm 90°$, and $\pm 150°$ relative to the beam direction, was used for the experiments in conjunction with a 14-element BGO multiplicity filter. The BGO multiplicity filter provided information on fold K and sum energy H for the cascading γ-ray transitions. In all four experiments, Pb-backed targets were used in order to improve the energy resolution for γ rays from low-lying states, which are emitted after the residual nuclei are stopped in the backing. An overall γ-ray energy resolution of full width at half maximum $\sim$2.2 keV was achieved at $\sim$550 keV. Targets of 2–3 mg/cm^2 thickness were used together with Pb backings sufficient to stop the recoiling residual nuclei. A summary of the experimental details is given in Table I.

III. DATA ANALYSIS AND RESULTS

The off-line data analyses including the construction of the level schemes and directional correlation from oriented states evaluations are discussed below for the individual nuclei. The software package RADWARE [12] was used throughout this process.

A. ^{128,130,132}Cs

The partial level schemes for ^{128,130,132}Cs are consolidated into Fig. 1. The measured properties of the γ-ray transitions in the level schemes are tabulated in Tables II, III, and IV. The γ-ray energies are accurate to $\pm$ 0.5 keV. Uncertainties on the relative intensities listed in the tables vary from 5% for strong transitions ($I_\gamma > 5$) up to 30% for weaker transitions.

The pulsed beams used in these experiments allowed the extraction of information on the distribution of time delays between the arrival of the beam pulse and detection of the γ rays. Time windows for prompt γ-γ coincidences were set at $\Delta t \approx 10$ ns; a time window of $\sim$100 ns was used for the ^{128}Cs isomer studies. The transition energy-time information was utilized to separate prompt from delayed events via two-dimensional E_γ vs t gating. Totals of approximately 54×10^6, 62×10^6, and 42×10^6 prompt γ-γ events collected in the ^{128}Cs, ^{130}Cs, and ^{132}Cs experiments, respectively, were sorted into E_γ-E_γ matrices.

The level schemes, presented in Fig. 1, were constructed on the basis of the observed coincidence relationships. The negative-parity bands are not shown in the level schemes, and will not be discussed since the current studies are fo-

TABLE II. Energies, intensities, and angular correlation data for transitions observed in ^{128}Cs. The γ-ray energies are accurate to ± 0.5 keV. Uncertainties on the relative intensities listed in the tables vary from 5% for strong transitions up to 30% for weaker transitions.

E_γ (keV)	I_γ (%)[a]	DCO Ratio[b]	I_i^π-I_f^π[c]	Multipolarity
142.8	100.0	0.49(6)	10^+-9^+	$M1/E2$
272.7	29.5	0.46(6)	12^+-11^+	$M1/E2$
348.6	64.1	0.40(6)	11^+-10^+	$M1/E2$
357.0	2.8		14^+-13^+	$M1/E2$
362.9	3.5		13^+-12^+	$M1/E2$
370.8	4.6		14^+-13^+	$M1/E2$
371.8	4.5	0.47(9)	12^+-11^+	$M1/E2$
408.0	30.2	0.40(5)	13^+-12^+	$M1/E2$
409.8	0.6		16^+-15^+	$M1/E2$
443.5	7.1		15^+-14^+	$M1/E2$
452.4	1.0		17^+-16^+	$M1/E2$
464.5	8.3	0.34(5)	15^+-14^+	$M1/E2$
493.1	2.5		17^+-16^+	$M1/E2$
508.9	27.3		11^+-10^+	$M1/E2$
532.0	13.2		12^+-11^+	$M1/E2$
554.2	5.9		13^+-12^+	$M1/E2$
571.1	11.5		14^+-13^+	$M1/E2$
621.6	42.5		12^+-10^+	$E2$
622.2	3.1		13^+-12^+	$M1/E2$
638.6	4.1		16^+-15^+	$M1/E2$
651.7	9.1		11^+-9^+	$E2$
681.1	5.5		13^+-11^+	$E2$
719.9	1.2		14^+-12^+	$E2$
735.0	8.8		13^+-11^+	$E2$
779.2	23.6	1.04(14)	14^+-12^+	$E2$
800.9	3.8		15^+-13^+	$E2$
835.5	6.4		15^+-13^+	$E2$
874.5	11.0	0.95(18)	16^+-14^+	$E2$
903.2	3.3		17^+-15^+	$E2$
903.3	1.1		16^+-14^+	$E2$
912.4	2.2		17^+-15^+	$E2$
930.7	4.4		18^+-16^+	$E2$
950.6	0.8		19^+-17^+	$E2$
986.8	1.3		20^+-18^+	$E2$

[a]Intensities are normalized to 100% for the 142.8-keV transition.
[b]DCO ratios listed here are obtained from gating on $\Delta I = 2$ $E2$ transitions.
[c]Proposed spin values are based on $I_0^\pi = 9^+$ for the bandhead spin (see text for details).

TABLE III. Energies, intensities, and angular correlation data for transitions observed in ^{130}Cs. The γ-ray energies are accurate to ± 0.5 keV. Uncertainties on the relative intensities listed in the tables vary from 5% for strong transitions up to 30% for weaker transitions.

E_γ (keV)	I_γ (%)[a]	DCO Ratio[b]	I_i^π-I_f^π[c]	Multipolarity
151.7	100.0	1.22(10)	10^+-9^+	$M1/E2$
289.9	42.2	0.88(8)	12^+-11^+	$M1/E2$
349.9	3.0		14^+-13^+	$M1/E2$
353.1	79.9	0.84(7)	11^+-10^+	$M1/E2$
371.9	3.0		13^+-12^+	$M1/E2$
400.9	5.6	0.82(12)	12^+-11^+	$M1/E2$
416.8	36.5	0.60(6)	13^+-12^+	$M1/E2$
426.3	8.9	0.80(11)	14^+-13^+	$M1/E2$
453.5	5.8	0.82(12)	15^+-14^+	$M1/E2$
465.7	1.0		16^+-15^+	$M1/E2$
468.5	8.8	0.73(10)	15^+-14^+	$M1/E2$
492.0	2.0		17^+-16^+	$M1/E2$
547.0	19.3	0.76(9)	11^+-10^+	$M1/E2$
574.2	6.5		13^+-12^+	$M1/E2$
595.1	17.1	0.55(7)	12^+-11^+	$M1/E2$
609.4	15.8	0.47(6)	14^+-13^+	$M1/E2$
643.5	26.8	1.85(20)	12^+-10^+	$E2$
676.6	1.6		13^+-12^+	$M1/E2$
698.9	4.8		11^+-9^+	$E2$
707.1	6.6	1.56(30)	13^+-11^+	$E2$
722.4	1.3		14^+-12^+	$E2$
773.3	5.3		13^+-11^+	$E2$
803.9	1.9		15^+-13^+	$E2$
843.8	20.3	1.80(20)	14^+-12^+	$E2$
895.8	8.1	1.69(31)	15^+-13^+	$E2$
934.2	7.1		16^+-14^+	$E2$
957.8	2.2		17^+-15^+	$E2$

[a]Intensities are normalized to 100% for the 151.7-keV transition.
[b]DCO ratios listed here are obtained by gating on the $\Delta I=1$ 409-keV $E1$ transition.
[c]Proposed spin values are based on $I_0^\pi=9^+$ for the bandhead spin (see text for details).

TABLE IV. Energies, intensities, and angular correlation data for transitions observed in ^{132}Cs. The γ-ray energies are accurate to ± 0.5 keV. Uncertainties on the relative intensities listed in the tables vary from 5% for strong transitions up to 30% for weaker transitions.

E_γ (keV)	I_γ (%)[a]	DCO Ratio[b]	I_i^π-I_f^π[c]	Multipolarity
147.0	10.8		12^+-11^+	$M1/E2$
150.7	100.0	1.10(10)	10^+-9^+	$M1/E2$
152.7	15.7		12^+-11^+	$M1/E2$
163.5	3.3		11^+-10^+	$M1/E2$
168.0	5.8		13^+-12^+	$M1/E2$
298.4	6.7		12^+-11^+	$M1/E2$
304.1	4.9		12^+-11^+	$M1/E2$
310.2	10.8		12^+-11^+	$M1/E2$
313.4	3.7		13^+-12^+	$M1/E2$
387.8	4.7		13^+-12^+	$M1/E2$
401.5	41.7	0.76(9)	11^+-10^+	$M1/E2$
407.8	26.0	2.47(37)	13^+-12^+	$M1/E2$
413.2	9.7		13^+-12^+	$M1/E2$
422.0	2.8		13^+-12^+	$M1/E2$
427.7	11.2		13^+-12^+	$M1/E2$
446.2	5.9		10^+-10^+	$M1/E2$
518.6	5.5		12^+-11^+	$M1/E2$
540.5	3.6		15^+-13^+	$E2$
553.3	16.7		11^+-10^+	$M1/E2$
609.9	18.7		11^+-10^+	$M1/E2$
700.2	23.0	1.90(30)	12^+-10^+	$E2$
704.1	28.0	2.12(37)	11^+-9^+	$E2$
706.0	21.1	1.75(33)	12^+-10^+	$E2$
760.5	2.6		11^+-9^+	$E2$
883.7	5.9		14^+-12^+	$E2$
994.4	12.2		15^+-13^+	$E2$
996.8	3.6		17^+-15^+	$E2$

[a]Intensities are normalized to 100% for the 150.7-keV transition.
[b]DCO ratios listed here are obtained by gating on the $\Delta I=1$ 594-keV $E1$ transition.
[c]Proposed spin values are based on $I_0^\pi=9^+$ for the bandhead spin (see text for details).

cused on the positive-parity $\pi h_{11/2}\otimes \nu h_{11/2}$ doublet bands.

The angular dependence of the γ-ray intensities was investigated using the methods of directional correlations from oriented states (DCO) [13] in order to determine the multipolarities of the γ-ray transitions. Asymmetric matrices were sorted by incrementing those events in which a coincidence between a γ ray detected at $\sim\pm 90°$ and another detected at either forward ($\sim\pm 30°$) or backward ($\sim\pm 150°$) angle occurred. By denoting the number of counts in a particular cell of the asymmetric matrix as $N_\gamma(x, y)$, the DCO ratio then is defined as

$$R_{DCO}=\frac{N_\gamma(E_{\gamma 1},E_{\gamma 2})}{N_\gamma(E_{\gamma 2},E_{\gamma 1})}, \tag{1}$$

where x and y are the energies of the coincident γ rays detected at forward/backward angles and at 90°, respectively. Throughout the paper, $E_{\gamma 2}$ refers to the gating transition.

The DCO analysis only allowed the determination of relative spins in the current studies. Since no transition connection to states with known spin has been established, absolute spin assignments for states in the positive-parity bands built on the $\pi h_{11/2}\otimes \nu h_{11/2}$ configuration could only be inferred from systematic studies of the $Z=55$ isotopic chain. As will be discussed in Sec. IV A 1, the systematics support bandhead spins $I_0^\pi=(9)^+$ for the yrast partner bands in all three isotopes.

1. ^{128}Cs level scheme

Partial results for ^{128}Cs from the present study have been reported in Ref. [3], for the purpose of a systematic comparison of the ^{128}Cs, ^{130}La, and ^{132}Pr nuclei. In addition to a

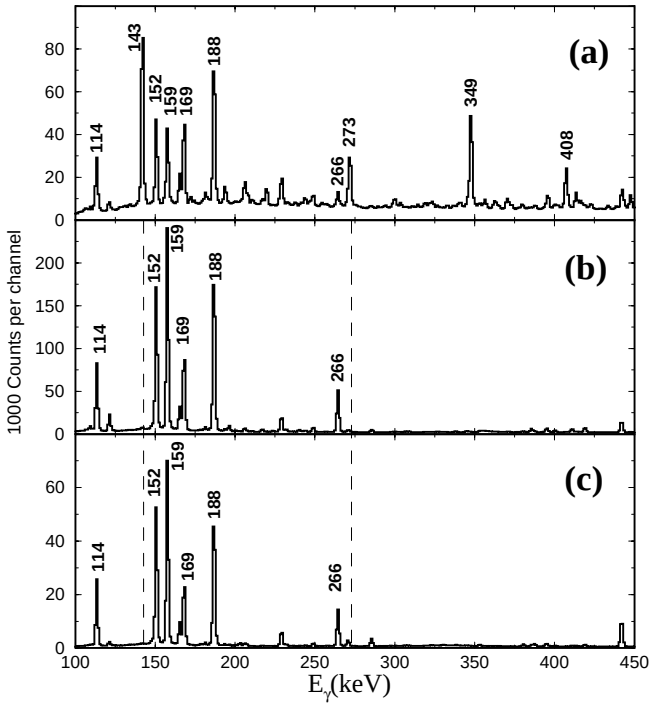

FIG. 2. (a) Total projection of prompt γ rays coincident with delayed transitions for ^{128}Cs. (b) Total projection of delayed γ rays coincident with prompt transitions. (c) Total projection of delayed-delayed coincident events. Absence of peaks at 143 keV and 273 keV in (b) and (c) are indicated with dashed lines.

newly identified sideband of the yrast band, the current work confirmed the existence of bands 1, 2, 3, and 4 as labeled in Ref. [14] with the exception of the 159- and 143-keV γ-ray ordering; this change in ordering affects the position of the known $T_{1/2} \approx 50$ ns isomeric state in ^{128}Cs. The proposed modification of the ^{128}Cs level scheme is made from the analysis of the time-gated energy spectra presented in Fig. 2. The top spectrum (a) shows the prompt γ rays coincident with the delayed γ rays; conversely, the spectrum (b) shows delayed transitions coincident with the prompt transitions.

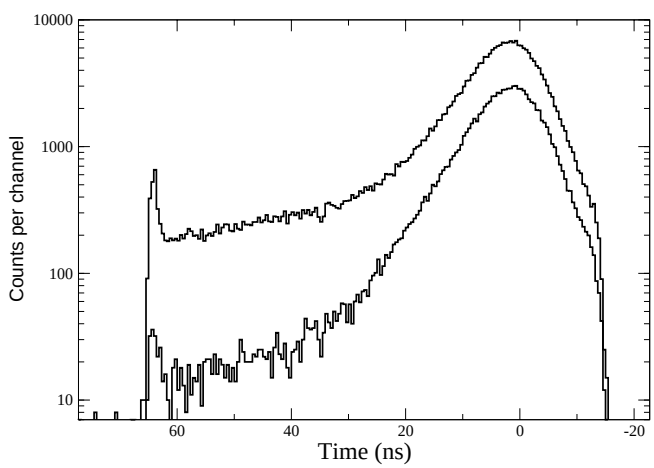

FIG. 3. Time spectrum of the 266-keV transition below the isomer (upper curve) in ^{128}Cs shown with that obtained by gating on the background near the peak (lower curve) for comparison.

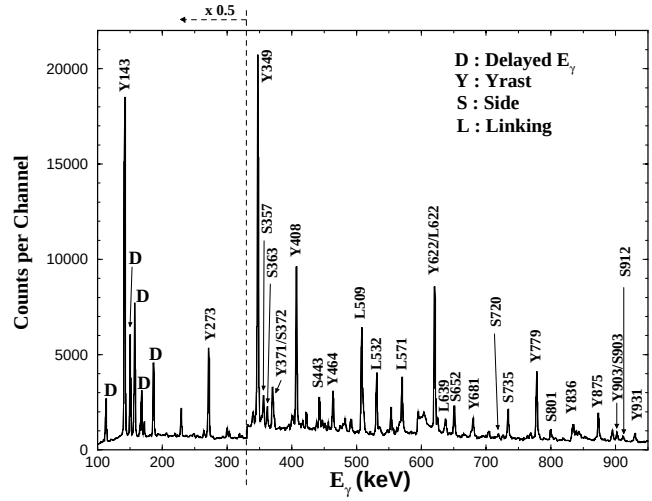

FIG. 4. Spectrum obtained by tagging on delayed transitions shows the yrast and sidebands in ^{128}Cs. Peaks labeled with a *D* correspond to delayed transitions below the isomer. Prompt transitions are labeled with their energies in keV, and are preceded by *Y*, *S*, or *L* for yrast, side, or linking transitions, respectively. Counts per channel have been halved for energies to the left of the dashed lines.

The panel (c) spectrum is the total projection of the delayed-delayed coincident matrix. The strong presence of the 143-keV γ ray in (a), but its absence in (b) and (c), shows that this transition is prompt and thus exists above the isomer. On the other hand, the reversed situation for the 159-keV γ ray places this transition below the isomer. As a result, the ordering of the two transitions are reversed from that proposed in Ref. [14], and the isomeric state is identified with the bandhead of the yrast band. These changes are consistent with the newly observed sideband *S*. The time profile of the 266-keV transition below the isomer is shown in Fig. 3 along with that of the prompt resolution function obtained by gating on prompt γ events of a similar energy. By tagging on these delayed γ transitions, it was possible to distinguish γ rays decaying into the isomer; only those transitions associated with the yrast and the sideband were observed to feed into the isomer, as shown in Fig. 4. (The intensity imbalance at the 11^+ state suggests some additional feeding. The same is true for the ^{130,132}Cs isotopes. See Tables II, III, and IV.)

Because of the importance of the parity and relative spin assignments for the present study, the assignments will be discussed in some detail below. These DCO ratios of known stretched quadrupole ($E2$) transitions gated with known stretched dipole ($E1$) or stretched quadrupole ($E2$) transi-

TABLE V. A comparison between experimental and calculated DCO ratios for known γ rays by gating on the $2^+ \rightarrow 0^+$ 443-keV $E2$ transition in ^{128}Xe. A spin alignment parameter $\sigma_I/I = 0.3$ was assumed for the calculation.

E_γ (keV)	$I_i^\pi \rightarrow I_f^\pi$		Expt. R_{DCO}	Calc. R_{DCO}
590	$4^+ \rightarrow 2^+$	$E2$	1.01(10)	1
704	$6^+ \rightarrow 4^+$	$E2$	0.96(10)	1
1196	$5^- \rightarrow 4^+$	$E1$	0.50(10)	0.54

TABLE VI. Experimental DCO ratios and calculated mixing ratios for the known $\Delta I=1$ $M1/E2$ transitions in the yrast $\pi h_{11/2} \otimes \nu h_{11/2}$ band in ^{128}Cs. $I_0=9$ is assumed for the bandhead spin (see text for details).

	$M1/E2$		$E2$ Gate		
E_γ (keV)	$I_i^\pi \rightarrow I_f^\pi$	δ	E_γ (keV)	$I_i^\pi \rightarrow I_f^\pi$	R_{DCO}
143	$10^+ \rightarrow 9^+$	$-0.05^{+0.06}_{-0.07}$	779	$14^+ \rightarrow 12^+$	0.49(6)
349	$11^+ \rightarrow 10^+$	$-0.16^{+0.07}_{-0.09}$	681	$13^+ \rightarrow 11^+$	0.40(6)
273	$12^+ \rightarrow 11^+$	$-0.09^{+0.05}_{-0.07}$	779	$14^+ \rightarrow 12^+$	0.46(6)
408	$13^+ \rightarrow 12^+$	$-0.17^{+0.06}_{-0.06}$	622	$12^+ \rightarrow 10^+$	0.40(5)
371	$14^+ \rightarrow 13^+$	$-0.09^{+0.09}_{-0.10}$	622	$12^+ \rightarrow 10^+$	0.47(9)
464	$15^+ \rightarrow 14^+$	$-0.25^{+0.07}_{-0.09}$	779	$14^+ \rightarrow 12^+$	0.34(5)

tions were extracted for transitions from the even-even ^{128}Xe nucleus populated via the $p3n$ channel. These DCO ratios are compared to values calculated for the experimental geometry [13]. These comparisons, summarized in Table V, show consistency between the calculated and experimental values. In ^{128}Cs, the DCO ratios for known $M1/E2$ yrast-member transitions were obtained by gating on stretched $E2$ transitions. Based on these values and known relative spin assignments, mixing ratios were calculated in a manner prescribed in Ref. [13]; the results are tabulated in Table VI. A spin alignment parameter $\sigma_I/I=0.3$ was assumed. Subsequently, DCO ratios of the linking γ rays, the 509-, 532-, 622-, 571-, and 639-keV transitions, were extracted by gating on the $M1/E2$ 143-, 349-, 273-, 408-, and 464-keV γ rays, respectively, as tabulated in Table VII. These experimental values were then used to determine multipolarities of the linking transitions. Figure 5 shows a comparison between the experimental and calculated R_{DCO} for the 509-keV γ ray. The areas defined by the limits of the gating-transition mixing ratio rule out all possibilities but the mixed $\Delta I=1$ $M1/E2$ character for the 509-keV linking transition. This follows from the calculations which show that for a gating γ transition with a negative mixing ratio only a $\Delta I=1$ $M1/E2$ multipolarity for the linking transitions gives $R_{DCO}<1$. As in Tables VI and VII, all of the gating γ rays but the 143-keV transition were found to have $\delta \leqslant 0$ and the corresponding R_{DCO} values for the linking transitions were all less than unity. The mixed $\Delta I=1$ $M1/E2$ multipolarity of all the linking transitions, therefore, ensures positive parity and the assigned relative spins for the sideband states.

TABLE VII. Experimental DCO ratios for transitions which link the sideband to the yrast band in ^{128}Cs. All gating transitions are of $\Delta I=1$ $M1/E2$ character. $I_0=9$ is assumed for the bandhead spin (see text for details).

Linking γ		Gating γ		
E_γ (keV)	$I_i^\pi \rightarrow I_f^\pi$	E_γ (keV)	$I_i^\pi \rightarrow I_f^\pi$	R_{DCO}
509	$11^+ \rightarrow 10^+$	143	$10^+ \rightarrow 9^+$	0.82(9)
532	$12^+ \rightarrow 11^+$	349	$11^+ \rightarrow 10^+$	0.87(10)
622	$13^+ \rightarrow 12^+$	273	$12^+ \rightarrow 11^+$	0.65(14)
571	$14^+ \rightarrow 13^+$	408	$13^+ \rightarrow 12^+$	0.86(13)
639	$16^+ \rightarrow 15^+$	464	$15^+ \rightarrow 14^+$	0.63(16)

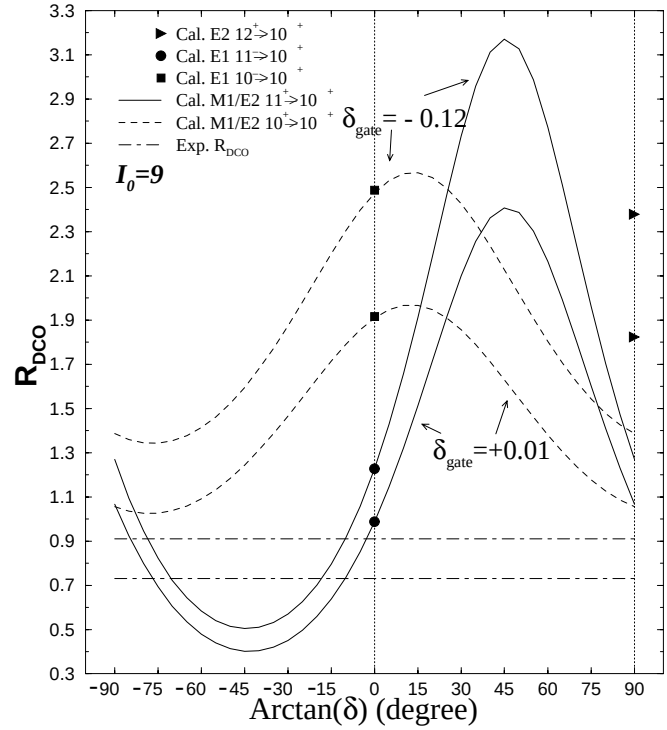

FIG. 5. Experimental and calculated DCO ratios as a function of mixing ratio δ for the 509-keV transition in ^{128}Cs. The gating transition was the 143-keV $\Delta I=1$ $M1/E2$ with $-0.12 \leqslant \delta_{gate} \leqslant +0.01$. The experimental upper and lower DCO values are indicated as dot-dashed lines, which overlap only with the calculated curves for a $\Delta I=1$ $M1/E2$ transition (solid curves).

2. ^{130}Cs level scheme

In the present study of ^{130}Cs, the yrast $\pi h_{11/2} \otimes \nu h_{11/2}$ band has been extended up to $I^\pi=(17^+)$, and a sideband decaying to the yrast band was observed for the first time; partial results were reported in Ref. [1]. The ^{130}Cs level scheme deduced by Sala *et al.* [15] for states above the 5^- $T_{1/2}=3.46$ min. isomeric state was confirmed. The 609-keV transition reported in Ref. [15] is an interband transition between the new sideband and yrast band in the current level scheme. Kumar *et al.* [16] confirmed and extended both the yrast and the sideband. They also observed additional linking transitions, which are too weak to be seen in the present work. A partial level scheme containing the sideband along with the yrast band is shown in Fig. 1. The coincidence spectra gated by the 401-, 372-, and 677-keV γ rays, which are relatively clean sideband γ rays, are shown in Fig. 6 as (a), (b), and (c), respectively. Panel (a) shows strong coincidences of the 401-keV transition with the 372-, 547-, and 699-keV γ rays. While the 152-keV γ ray in the yrast band is evident in the spectra, the rest of the dipole transitions above the 152-keV transition are absent. In panel (b), the strong presence of the 595-keV γ ray together with the 353- and 152-keV γ rays can be seen. Also the 350- and 804-keV γ transitions, both of which feed the $(13)^+$ member of the

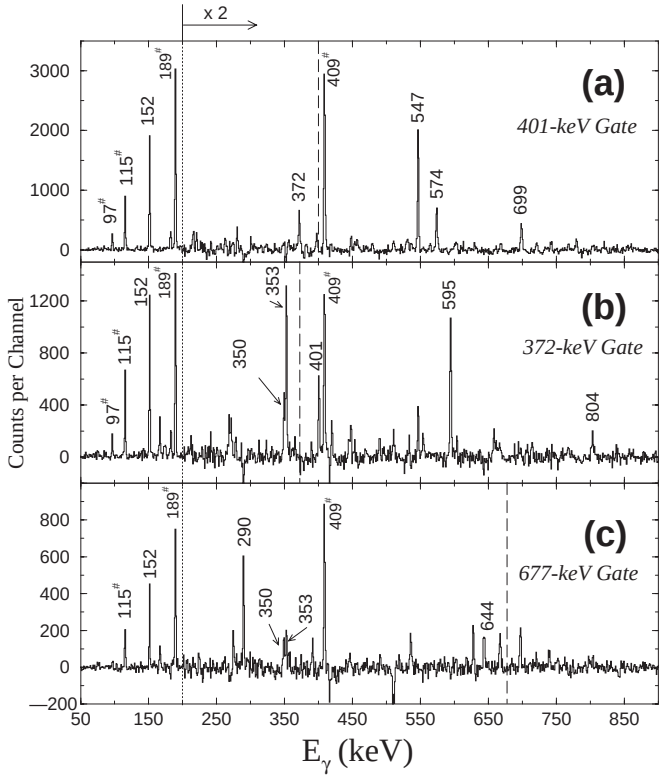

FIG. 6. Spectra gated on (a) 401, (b) 372, and (c) 677 keV, showing the sideband transitions in ^{130}Cs. Dashed vertical lines are positions of the gating transitions. Peaks marked with # are part of the series of γ rays below the $\pi h_{11/2} \otimes \nu h_{11/2}$ bandhead, I_0; these transitions are not shown in the level scheme in Fig. 1. Counts per channel have been doubled for energies to the right of the dotted line. Peaks are labeled with their energies in keV.

sideband, are present. Panel (c) defines the 677-keV link between the $(13)^+$ state in the sideband and the $(12)^+$ state in the yrast band, via the 290-, 353-, 644-, and 152-keV γ transitions.

Mixing ratios of the known $\Delta I=1$ $M1/E2$ yrast band transitions, namely, the 152-, 353-, 290-, and 417-keV transitions, were calculated based on the experimental DCO ratios in a manner similar to the ^{128}Cs analysis (see Table VIII). These DCO ratios of the linking transitions were obtained by gating on the mixed $M1/E2$ γ transitions and are summarized in Table IX; these values were then compared with calculated R_{DCO} using the calculated mixing ratio of the gating transitions. Figure 7 shows the experimental R_{DCO} of the 547-keV link for the 152-keV gating; an overlap with the calculated R_{DCO} occured only for a $\Delta I=1$ $M1/E2$ transition which determines uniquely its multipolarity. For the 152-keV γ ray, the R_{DCO} value was obtained either by gating on a stretched quadrupole or a stretched dipole transition. The lower and upper limit for the mixing ratio δ of the 152-keV gating transition was $+0.05$ and $+0.17$, respectively. For other links, again R_{DCO} values smaller than unity were extracted from gates on $\Delta I=1$ $M1/E2$ transitions with $\delta \leqslant 0$. Therefore, the relative spins and positive parity were assigned to the sideband of ^{130}Cs as presented in the level scheme in Fig. 1. These assignments are consistent with the

TABLE VIII. Experimental DCO ratios and calculated mixing ratios for the known $\Delta I=1$ $M1/E2$ transitions in the yrast $\pi h_{11/2} \otimes \nu h_{11/2}$ band in ^{130}Cs. $I_0=9$ is assumed for the bandhead spin (see text for details).

	$M1/E2$		Gate		
E_γ (keV)	$I_i^\pi \rightarrow I_f^\pi$	δ	E_γ (keV)	$I_i^\pi \rightarrow I_f^\pi$	R_{DCO}
152	$10^+ \rightarrow 9^+$	$+0.11^{+0.05}_{-0.06}$	644	$12^+ \rightarrow 10^+$	0.66(7)
		$+0.12^{+0.05}_{-0.05}$	409[a]	$10^+ \rightarrow 9^-$	1.22(10)
353	$11^+ \rightarrow 10^+$	$-0.09^{+0.07}_{-0.08}$	844	$14^+ \rightarrow 12^+$	0.45(7)
290	$12^+ \rightarrow 11^+$	$-0.05^{+0.05}_{-0.07}$	844	$14^+ \rightarrow 12^+$	0.48(6)
417	$13^+ \rightarrow 12^+$	$-0.14^{+0.06}_{-0.06}$	644	$12^+ \rightarrow 10^+$	0.41(5)

[a]Not shown in Fig. 1.

DCO ratios for the in-band transitions of the sideband obtained, where possible, by gating on the intense 409-keV[2] $(9)^+ \rightarrow (8)^-$ dipole (see Table III).

3. ^{132}Cs level scheme

The partial level scheme of ^{132}Cs shown in Fig. 1 shows the sideband $S1$, discovered in the current work, as well as a series of positive-parity states labeled as $S2$, which have been reported by Hayakawa *et al.* in Ref. [17]. The present study confirms the level scheme proposed for ^{132}Cs in Ref. [17] for states above the (7^-) state, except the $(13^+) \rightarrow (11^+)$ 726-keV γ ray in band 3 [17] was not observed. In addition to the 147-keV transition previously reported, which links the (12^+) state in the band Y to the (11^+) state in $S2$, the 422-keV links between the (13^+) state in Y and the (12^+) state in $S2$ was observed in this work. Spectra obtained by gating on relatively clean sideband $S1$ transitions are shown in Fig. 8.

As in the previous two isotopes, mixing ratios for the $\Delta I=1$ $M1/E2$ members of band Y were calculated based on the experimental DCO ratios. (The $\pi h_{11/2} \otimes \nu h_{11/2}$ configuration is no longer yrast in ^{132}Cs, although it is lowest in energy for a given spin among positive-parity bands; thus it is still labeled as band Y in the level scheme.) For the $(10^+) \rightarrow (9^+)$ 151-keV γ ray, R_{DCO} values were extracted by gating on the $(9^+) \rightarrow (8^-)$ 594-keV, $(9^+) \rightarrow (9^-)$ 343-keV (these transitions are not shown in the level scheme), and $(12^+) \rightarrow (10^+)$ 700-keV γ rays; these results placed an upper limit on the mixing ratio of $\delta \leqslant +0.08$ (see Table X). It is not possible to determine whether this transition is $\Delta I=1$ $E1$ or $M1/E2$ from the measured DCO ratios alone; however, the former is unlikely based on the systematics of the $\pi h_{11/2} \otimes \nu h_{11/2}$ bands in the Cs isotopes [8]. A mixing ratio $\delta < 0$ was calculated from R_{DCO} values for the $(11^+) \rightarrow (10^+)$ 402-keV transition.[3] These DCO ratios for the link-

[2]Not shown in Fig. 1.

[3]The 594- and 343-keV transitions were used as gates for the extraction of R_{DCO} for the 402-keV transition. The 402-keV transition is not directly above these gating transition with the 151-keV transition in between. Thus, in calculating the mixing ratio for the 402-keV transition in the three γ-ray cascade transition, the 151-

TABLE IX. Experimental DCO ratios for transitions which link the sideband to the yrast band in ^{130}Cs. All gating transitions are of $\Delta I=1$ $M1/E2$ character. $I_0=9$ is assumed for the bandhead spin (see text for details).

Linking γ E_γ (keV)	$I_i^\pi \rightarrow I_f^\pi$	Gating γ E_γ (keV)	$I_i^\pi \rightarrow I_f^\pi$	R_{DCO}
547	$11^+ \rightarrow 10^+$	152	$10^+ \rightarrow 9^+$	0.58(6)
595	$12^+ \rightarrow 11^+$	353	$11^+ \rightarrow 10^+$	0.73(8)
677	$13^+ \rightarrow 12^+$	290	$12^+ \rightarrow 11^+$	0.67(19)
609	$14^+ \rightarrow 13^+$	417	$13^+ \rightarrow 12^+$	0.87(11)

ing transitions between the two sidebands and band Y, namely, the $(S1)$610-, $(S2)$553-, and $(S1)$519-keV γ rays, were obtained by gating on the aforementioned 151- and 402-keV transitions, and are presented in Table XI. These measured values were then compared to the calculated R_{DCO} values, as representatively shown in Fig. 9 for the 610- and 553-keV linking transitions. The comparison implies a $\Delta I=1$ $M1/E2$ multipolarity for the $(S1)$ 610- and $(S1)$ 519-keV transitions, thus making the band $S1$ positive parity and having relative spins as shown in the level scheme in Fig. 1. Although a $\Delta I=1$ $E1$ transition cannot be ruled out for the $(S2)$ 553-keV transition connecting the bands $S2$ and Y, a mixed $\Delta I=1$ $M1/E2$ multipolarity was assigned to the 553-keV decay as being more likely, as was proposed in Ref. [17].

keV mixing ratio was varied within uncertainties as listed in Table X.

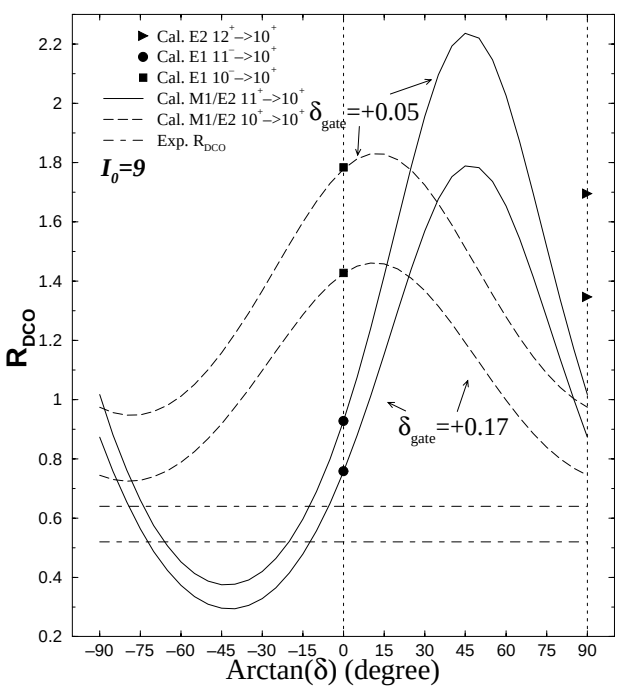

FIG. 7. Experimental and calculated DCO ratios as a function of mixing ratio δ for the 547-keV transition in ^{130}Cs. The gating transition was the 152-keV $\Delta I=1$ $M1/E2$ with $+0.05 \leqslant \delta_{gate} \leqslant +0.17$. The experimental upper and lower DCO values are indicated as dot-dashed lines, which overlap only with the calculated curves for a $\Delta I=1$ $M1/E2$ multipolarity (solid curves).

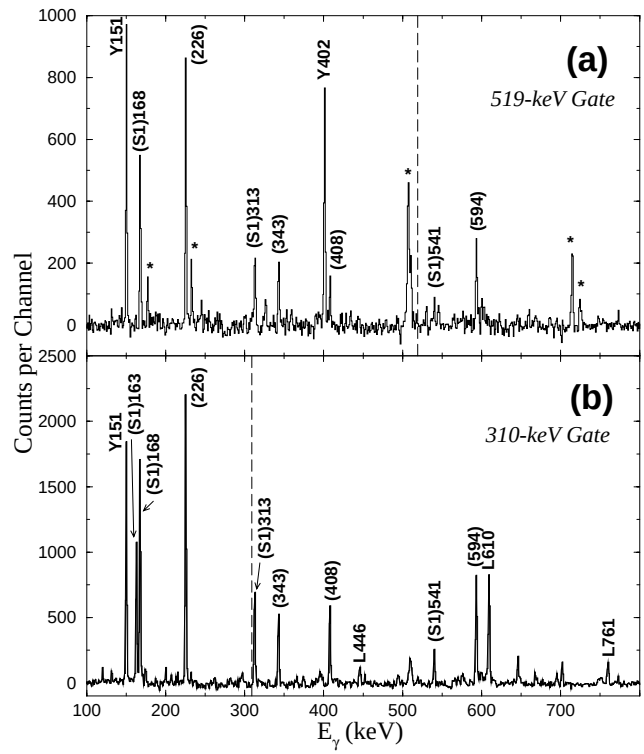

FIG. 8. Spectra gated on (a) 519-keV and (b) 310-keV showing the sideband transitions in ^{132}Cs. Dashed vertical lines are positions of the gating transitions. Peaks are labeled with energies in keV, and are preceded by Y, $(S1)$, or L for the main band, $S1$, or linking transitions, respectively. Peaks marked with * are contaminants. Those peaks marked with their energies in parentheses are not shown in Fig. 1.

B. ^{134}Cs

The level scheme deduced for ^{134}Cs from the present work is shown in Fig. 10. An extensive study on low-lying states in this nucleus, produced through thermal neutron cap-

TABLE X. Experimental DCO ratios and calculated mixing ratios for the known $\Delta I=1$ $M1/E2$ transitions in the yrast $\pi h_{11/2} \otimes \nu h_{11/2}$ band in ^{132}Cs. $I_0=9$ is assumed for the bandhead spin (see text for details).

E_γ (keV)	$M1/E2$ $I_i^\pi \rightarrow I_f^\pi$	δ	Gate E_γ (keV)	$I_i^\pi \rightarrow I_f^\pi$	R_{DCO}
151	$10^+ \rightarrow 9^+$	$+0.03^{+0.05}_{-0.06}$	594[a]	$9^+ \rightarrow 8^-$	1.06(10)
		$+0.03^{+0.05}_{-0.06}$	343[a]	$9^+ \rightarrow 9^-$	0.54(6)
		$-0.03^{+0.06}_{-0.06}$	700	$12^+ \rightarrow 10^+$	0.51(6)
402[b]	$11^+ \rightarrow 10^+$	$-0.08^{+0.07}_{-0.08}$	594	$9^+ \rightarrow 8^-$	0.87(11)
		$-0.12^{+0.07}_{-0.10}$	343	$9^+ \rightarrow 9^-$	0.40(7)

[a]Not shown in Fig. 1.
[b]Mixing ratios were calculated using three transition cascades.

TABLE XI. Experimental DCO ratios for transitions which link the sideband to the yrast band in ^{132}Cs. All gating transitions are of $\Delta I=1$ $M1/E2$ character. $I_0=9$ is assumed for the bandhead spin (see text for details).

Linking γ E_γ (keV)	$I_i^\pi \rightarrow I_f^\pi$	Gating γ E_γ (keV)	$I_i^\pi \rightarrow I_f^\pi$	R_{DCO}
610 ($S1$)	$11^+ \rightarrow 10^+$	151	$10^+ \rightarrow 9^+$	0.61(9)
553 ($S2$)	$11^+ \rightarrow 10^+$	151	$10^+ \rightarrow 9^+$	0.84(11)
519 ($S1$)	$12^+ \rightarrow 11^+$	402	$11^+ \rightarrow 10^+$	0.86(12)

ture, was reported earlier by Bogdanović *et al.* [18]; however, no information on high-spin states has been previously reported. Therefore, the identification of the high-spin states associated with ^{134}Cs is discussed in detail below.

Approximately 40×10^6 γ-γ coincidence events were sorted into symmetric E_γ-E_γ matrices for the 28-MeV and 33-MeV ^{7}Li beam energies. In addition, γ-γ events with a multiplicity ball condition $K>4$ with the 28-MeV run were sorted into another matrix to enhance the $3n$ evaporation channel. Total projections of the three aforementioned matrices are shown in Fig. 11. A strong peak at 366-keV from ^{133}Cs serves as a reference. The relative heights of the 206- and 296-keV peaks against that of the reference show a significant increase in the projection (b) at 28 MeV compared to those in (a) at 33 MeV. In the fold-gated projection (c), the three peaks are comparable in height. Ratios of fitted peak intensities to that of the 366-keV reference in each spectrum are plotted in Fig. 12. The dashed-dotted lines are for γ rays in ^{131}I ($\alpha 2n$ channel), and the dotted lines are for γ rays in ^{133}Cs ($4n$ channel). The cross sections for γ rays of unknown origins, which are proposed to be in ^{134}Cs in the present work, are drawn as solid lines in Fig. 12. Additional evidence that these unknown γ rays are not associated with ^{133}Cs comes from the ^{130}Te(^{6}Li, $4n$) ^{132}Cs reaction at a

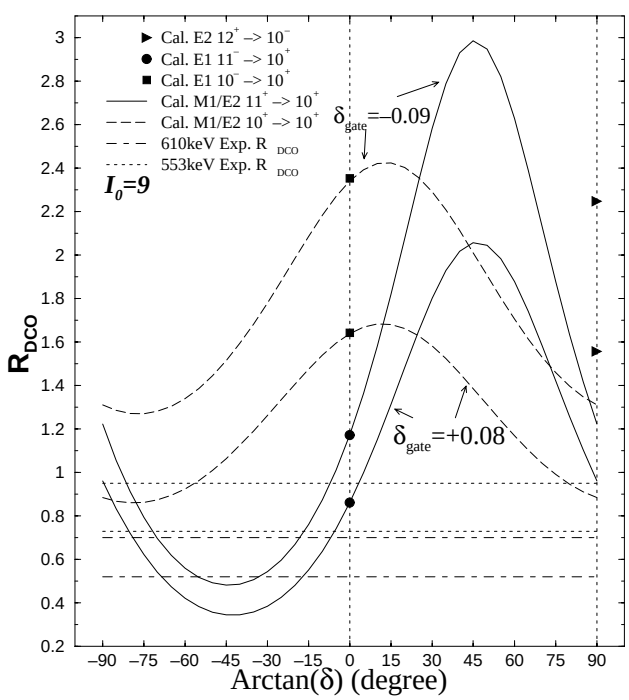

FIG. 9. Experimental and calculated DCO ratios as a function of mixing ratio δ for the 610- and 553-keV transitions in ^{132}Cs. The gating transition was the 151-keV $\Delta I=1$ $M1/E2$ with $-0.09 \leqslant \delta_{gate} \leqslant +0.08$. The experimental upper and lower DCO values are indicated as dotted lines for the 553-keV transition and dot-dashed lines for the 610-keV transition. See text for details.

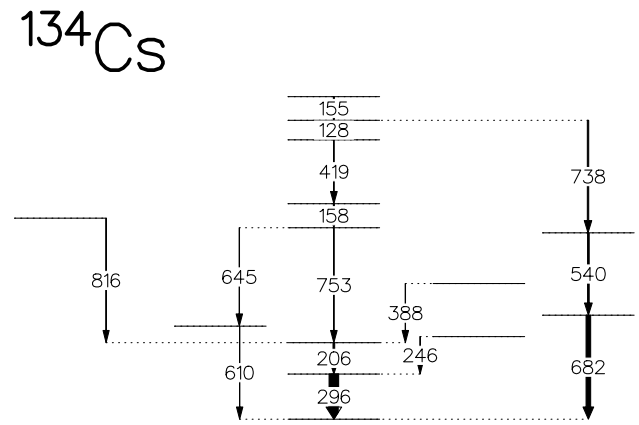

FIG. 10. Level scheme of ^{134}Cs deduced from γ-γ coincidence measurements in this work. Spins and parities could not be assigned.

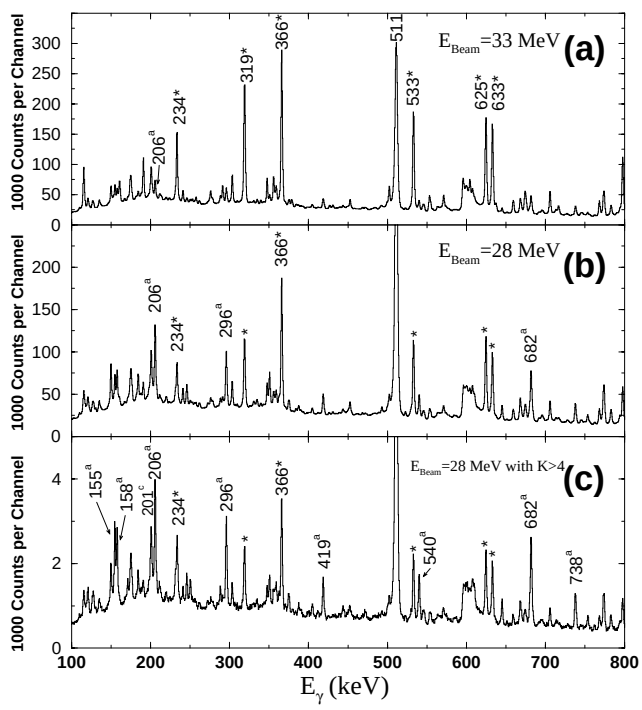

FIG. 11. (a) Total coincident projection in the ^{130}Te(^{7}Li, xn) reaction at $E_{beam}=33$ MeV. (b) Total projection from the same reaction, but at $E_{beam}=28$ MeV. (c) Total projection with the same reaction and beam energy as in (b), but gated on multiplicity $K>4$. The 201-keV peak labeled with c could not be placed. Peaks marked with * are in the $4n$ channel which leads to ^{133}Cs, while those marked with a are proposed to be in the $3n$ channel corresponding to ^{134}Cs.

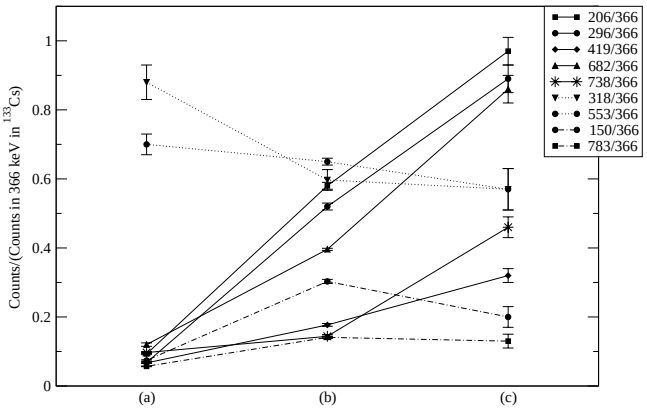

FIG. 12. Relative intensities of γ transitions (a) at $E_{beam}=33$ MeV, (b) at 28 MeV, and (c) at 28 MeV with $K>4$ gating. The ratios are of the fitted intensity of a γ peak over that of the strong 366-keV transition in ^{133}Cs. Points connected by solid lines are proposed to represent transitions in ^{134}Cs$(3n)$, whereas those connected by dotted and dash-dotted lines are obtained from transitions in ^{133}Cs$(4n)$ and ^{131}I$(\alpha 2n)$, respectively.

beam energy of 38 MeV; the 206- and 296-keV γ rays were not present in these data, while the known ^{133}Cs γ rays from the $3n$ channel were.

IV. DISCUSSION OF EXPERIMENTAL OBSERVABLES

A. Systematics of experimental observables in positive-parity bands

1. Excitation energy systematics and absolute spin assignments

Determination of absolute spins for rotational band members, whose decay paths to the ground state are highly fragmented or delayed by isomeric transitions, is difficult. Moreover, decay transitions of a few tens of keV are often highly electron converted. Absolute spin assignments are not possible in the current experiment. On the other hand, such information is crucial when a spin-dependent phenomenon such as the odd-/even-spin dependence of the quantity $S(I)$ is being investigated. In fact, discrepancies regarding assigned spins of the $\pi h_{11/2}\otimes\nu h_{11/2}$ band members, among the odd-odd Cs isotopes as well as neighboring odd-odd nuclei in the $A\sim 130$ region, motivated Liu *et al.* to reevaluate these assignments through a systematic study of the band excitation energies in $^{118-132}$Cs [8]. The observation of the additional $\Delta I=1$ sidebands in the odd-odd $^{128-132}$Cs isotopes from the present work, as well as in ^{126}Cs from Ref. [19], and in ^{124}Cs from Ref. [20], augments the systematics of the main bands, as presented in Fig. 13. The smooth change in the excitation energies for the sidebands provides strong evidence that the I_0 value, which is the basis of the relative spin assignment in Fig. 1 and also in Ref. [8] for $^{124-132}$Cs, shares the same spin value. Recognizing the importance of reliable spin assignments in the odd-odd Cs isotopes, Gizon *et al.* [20] studied ^{124}Cs by an in-beam γ-e^- coincidence experiment. Electron conversion coefficients were measured for the main low-lying transitions, and multipolarities were deduced accordingly. This study assigned $I_0^\pi=9^+$, which agrees with the value quoted in Ref. [8] based on the ^{130}Cs experiment by Sala *et al.* [15]. Moon *et al.*, however, have proposed $I_0^\pi=11^+$ in ^{120}Cs [21] and ^{122}Cs [22]. In their experiments, low-energy γ rays were detected by a low-energy photon spectrometer, and the decay sequence leading to an isomer with known spin was identified. Multipolarities for these transitions were then deduced from observed DCO ratios. These conflicting spin assignments remain to be resolved, although the discrepancy in spin by $2\hbar$ between the two assignments do not alter overall systematic trends discussed in this paper. Because of the completeness and techniques of the Ref. [20] study as well as the systematics of Ref. [8], the value $I_0^\pi=9^+$ will be adopted. Spin values discussed in this paper are denoted as $I_0+\Delta i$ ($\Delta i=0,1,2,3,\ldots$) except when comparisons between the experiment and model calculations demand absolute spin assignments, as in Sec. V B.

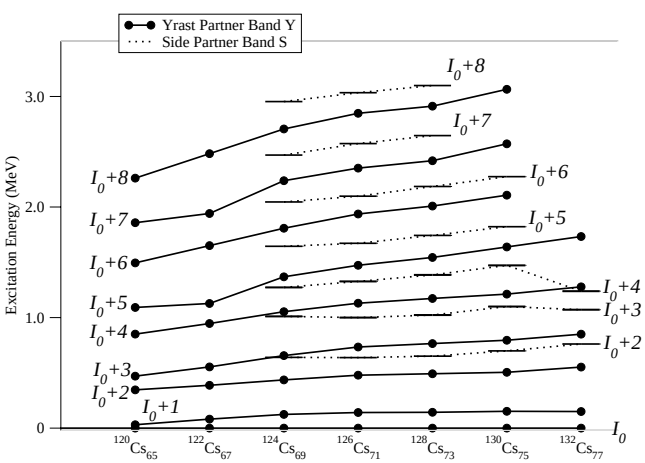

FIG. 13. Experimental excitation energies of the yrast and sideband members relative to the reference I_0 as a function of neutron number N. Closed circles connected by solid lines are for the yrast partner band denoted as Y, and horizontal bars connected by dotted lines are for the side partner band denoted as S. This choice coincides with that in Ref. [8] for $I_0=9$. The sideband information for ^{126,124}Cs is from Refs. [19,20].

2. Degeneracy between partner bands: Chiral doublets

The mechanism involved in the coupling of the three angular momenta into a chiral geometry was outlined in the Introduction. In essence, the chiral geometry minimizes the total energy for a given spin. This leads to a two-fold degeneracy in the energy eigenvalue; the corresponding energy eigenstates or solutions are denoted as $|\mathcal{L}\rangle$ and $|\mathcal{R}\rangle$. The total nuclear Hamiltonian is invariant under the chiral operator $\mathcal{T}\mathcal{R}_y(\pi)$,

$$[H,\mathcal{T}\mathcal{R}_y(\pi)]=0, \tag{2}$$

where $\mathcal{T}$ represents time reversal and $\mathcal{R}_y(\pi)$ a rotation about the intrinsic y axis by 180°. However, under the $\mathcal{T}\mathcal{R}_y(\pi)$ operator,

$$\mathcal{T}\mathcal{R}_y(\pi)|\mathcal{L}\rangle=|\mathcal{R}\rangle, \tag{3}$$

and

$$\mathcal{T}R_y(\pi)|\mathcal{R}\rangle = |\mathcal{L}\rangle. \tag{4}$$

Since chiral symmetry, which is preserved by the Hamiltonian, is broken for these solutions, the formation of the chiral geometry in the intrinsic frame of rotating nuclei is an example of so-called *spontaneous symmetry breaking* [23].

In the ideal case of strong symmetry breaking, i.e., $\langle \mathcal{L}|H|\mathcal{R}\rangle = \langle \mathcal{R}|H|\mathcal{L}\rangle^* = 0$, any linear combination of the two is an eigen solution. However, those which can be observed in the laboratory frame are invariant under the chiral operator and given as

$$|+\rangle = 1/\sqrt{2}\ (|\mathcal{R}\rangle + |\mathcal{L}\rangle),$$

$$|-\rangle = i/\sqrt{2}\ (|\mathcal{R}\rangle - |\mathcal{L}\rangle), \tag{5}$$

where

$$\mathcal{T}R_y(\pi)|+\rangle = |+\rangle,$$

$$\mathcal{T}R_y(\pi)|-\rangle = |-\rangle. \tag{6}$$

(See Ref. [24] for detailed discussion.) The time reversal operator is antiunitary involving complex conjugation. The $|\mathcal{L}\rangle$ and $|\mathcal{R}\rangle$ wave functions are, therefore, necessarily complex in order to be transformed to one another by $\mathcal{T}R_y(\pi)$. Each state with spin I in the rotational band is two-fold degenerate, and it cannot be associated with either purely left- or purely right-handed solution.

Weak symmetry breaking, however, occurs when the degeneracy is lifted via nonzero $\langle \mathcal{L}|H|\mathcal{R}\rangle = \langle \mathcal{R}|H|\mathcal{L}\rangle^*$. These off-diagonal matrix elements represent perturbations to a chiral geometry, namely, an admixture of nonchiral (planar) component in the otherwise pure $|\mathcal{L}\rangle$ and $|\mathcal{R}\rangle$ wave functions. It is important to emphasize that chiral geometry formation is a dynamical process as a function of spin. Even for an ideal chiral nucleus, the core rotation is small near the bandhead of the doublet bands leading to the total angular momentum confined close to the plane spanned by the single proton and neutron angular momenta. Thus, the two doublet bands cannot be inherently degenerate near the bandhead. The degree of symmetry breaking evolves with spin from weak to strong as the core angular momentum increases from small to larger values relative to the orbital angular momenta. Besides this *inherent* planar component at the lower spin, there are additional contributions to the planar part specific to individual nuclei. For example, a deviation of the core shape from maximum triaxiality (e.g., γ vibration) would destabilize the orientation of the core rotation along the intermediate axis. Another situation could be that Fermi levels are less favorable for the valence proton and neutron to be treated as a particle-hole configuration. Moreover, as in the case of the Cs isotopes, these factors are not independent by themselves, but interfere with each other. These *external* contributions to the inherent planar component could prevent the achievement of level degeneracy and thus strong symmetry breaking also at higher spin in the doublet bands.

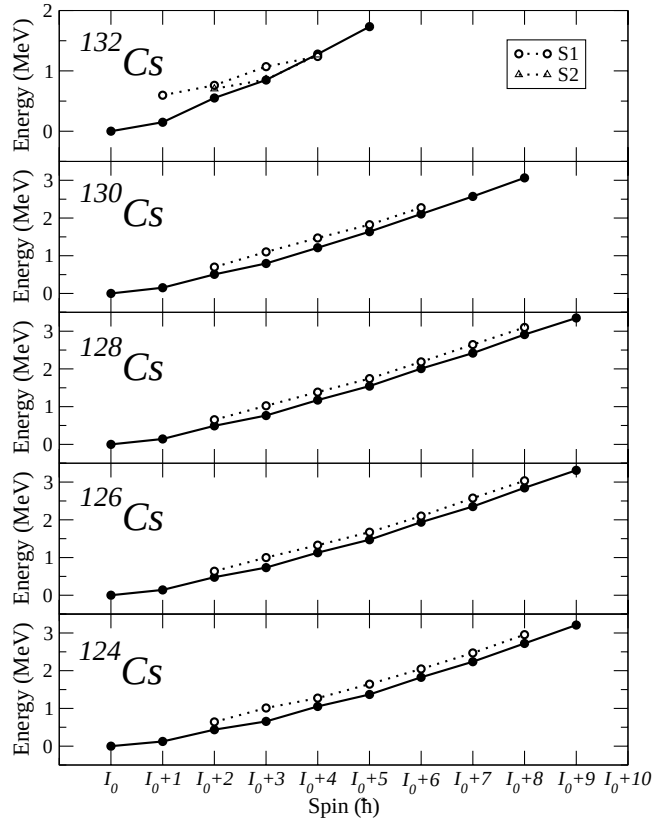

FIG. 14. Excitation energy vs spin for odd-odd $^{132-124}$Cs. Closed (open) circles connected by solid (dotted) lines are for the main band Y (the sideband S). For ^{132}Cs, two sidebands, $S1$ and $S2$, are included and the energy axis has a different scale from the rest.

Indeed, this appears to be the case for the Cs isotopes. The degree of degeneracy of the two bands for the $^{124-132}$Cs isotopes is indicated by the excitation energies of the band members as a function of spin, shown in Fig. 14. Except for ^{132}Cs, which will be discussed separately in Sec. IV B, the two curves maintain a roughly constant energy difference over the $^{126-130}$Cs isotopes. As argued in Refs. [1,9], a separation of $\lesssim$ 300 keV is too small for the sidebands to be interpreted as a band built either on the unfavored signature of the proton j_π orbital, or on the γ-phonon excitation. The chiral geometry in $^{124-132}$Cs will be argued as the cause of the nearly degenerate doublet bands.

3. Odd-/even-spin dependence of $S(I)=[E(I)-E(I-1)]/2I$

Since the signature quantum number is not a good quantum number for tilted axis cranking as required for aplanar triaxial geometries, the quantity $S(I)$ is introduced as the appropriate replacement. Its relation to the signature quantum number for axial principal axis cranking (PAC) will be discussed to explain this replacement.

A wealth of experimental information already available for the yrast $\pi h_{11/2} \otimes \nu h_{11/2}$ bands in this $A \sim 130$ region prior to the chiral doublet search owes its existence, in large part, to the study of the so-called signature inversion phenomenon. The signature quantum number is extensively used to

classify $\Delta I=2$ bands since it is a good quantum number in the limit of PAC where the wave function is invariant under $R_x(\pi)$, a rotation by 180° around the x axis. The eigenenergy states of opposite signature are degenerate when the cranking frequency ω is equal to zero, but for nonzero ω values, the degeneracy is lifted resulting in the so-called favored and unfavored signatures.

As first-order perturbation theory illustrates, the contribution from the Coriolis interaction to the Routhian is the well-known $-\hbar\omega\langle j_x\rangle$ term for small ω; the signature states are approximated by the linear combination $c(|j,\Omega\rangle \pm |j,-\Omega\rangle)$ where c is the phase and Ω is the projection of j on the symmetry axis. The expectation value $\langle j_x\rangle$ is nonzero, with opposite signs for each signature when the wave function has an $\Omega=1/2$ component. For axially symmetric odd-odd nuclei, the favored signature of a rotational band is given as $\alpha_f=\frac{1}{2}[(-1)^{j_\pi-1/2}+(-1)^{j_\nu-1/2}]$, where the total angular momentum I is related to α_f by $I=\alpha_f+2n$ ($n=0,1,2,3,\ldots$). In the case of the $\pi h_{11/2}\otimes\nu h_{11/2}$ configuration, $\alpha_f=1$, and the favored signature band members have odd spin. However, in the odd-odd $^{118-132}$Cs isotopes, it has been observed for lower spins that the favored ($\alpha_f=1$) signature members lie higher in excitation energy than the expected unfavored ($\alpha_u=0$) members. In $^{118-126}$Cs, this trend continues up to some critical spin I_c, after which the signature ordering expected for axial symmetry is restored. The quantity $S(I)=(1/2I)[E(I)-E(I-1)]$ is often used[4] to present signature changes such as the inversion phenomenon. (For a recent discussion of the subject see the paper by Riedinger *et al.* [25].)

Tajima [26] performed systematic calculations on odd-odd $^{124-130}$Cs isotopes in an attempt to reproduce the experimental features based on a particle-rotor model. A triaxial rigid rotor with an irrotational-flow moment of inertia and the inclusion of proton-neutron interactions were shown to be key factors for obtaining agreement with the experimental results in ^{124}Cs. It was also pointed out that the lack of rigorous spin assignments in the mass 130 region made comparisons between theory and experiments difficult.

Because the focus of the current study is to investigate the observed systematic properties on the basis of chiral geometry and triaxiality, caution must be taken in discussing the properties associated with $S(I)$. In axial PAC, there exists a direct one to one correspondence between signature (symmetry of the intrinsic system) and total angular momentum (a good quantum number in the laboratory frame); therefore, the experimental behavior of $S(I)$ in terms of signature is justified. However, the correspondence no longer holds for TAC in a triaxial nucleus. The grouping of excited states in terms of a signature quantum number is inappropriate in this case [26]. Hereafter in this paper, what is conventionally termed as signature inversion in the $A\sim130$ region is more appropriately discussed as an odd-/even-spin dependence of the quantity $S(I)$.

[4]This definition of $S(I)$ depends explicitly on spin, unlike an alternative definition, $S(I)=[E(I)-E(I-1)]-\frac{1}{2}[E(I+1)-E(I)+E(I-1)-E(I-2)]$. The latter, however, requires four energy levels as opposed to two in the former definition. Since the sidebands, involving fewer energy levels, are less developed than the main bands, the former definition is preferred in this study.

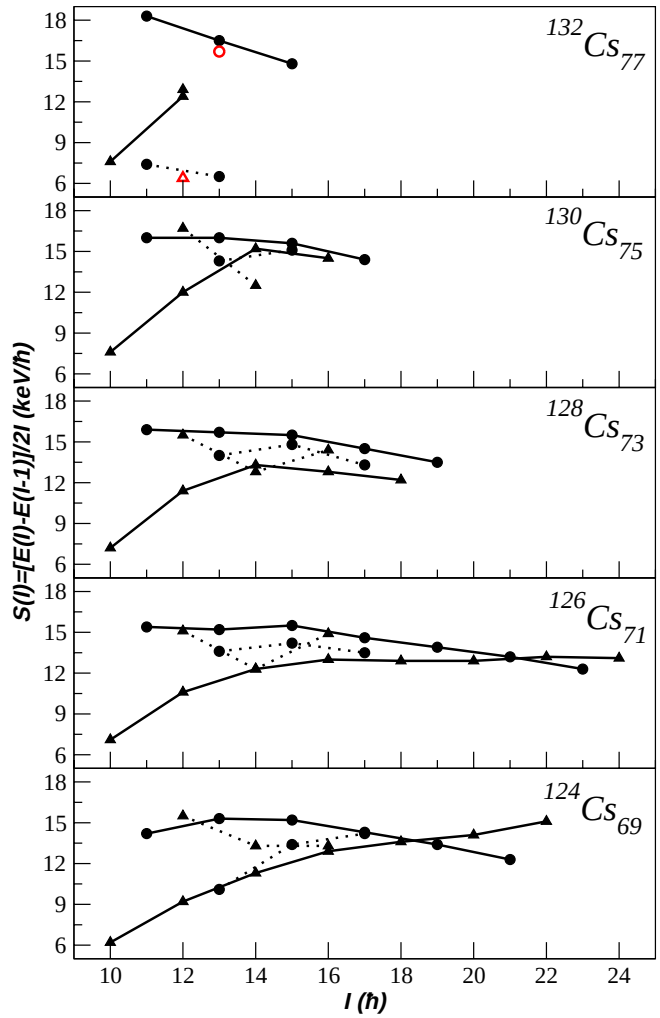

FIG. 15. $S(I)=1/2I[E(I)-E(I-1)]$ vs I for the main and the sideband in odd-odd $^{132-124}$Cs. Filled circles(triangles) are for odd(even)-spin sequence. $I_0^\pi=9^+$ was assumed for the bandhead spin. See the text for details. Points connected by solid lines are for the main band, while those connected by dotted lines are for the sideband. The open circle and triangle in the ^{132}Cs plot are for the sideband denoted as $S2$ in Fig. 1.

In Fig. 15, $S(I_{even})$ and $S(I_{odd})$ are plotted for the doublet bands in $^{124-132}$Cs. (Due to the sparcity of data for the sideband in ^{132}Cs, it will be excluded from the discussion below.) Although the even-spin states are consistently favored in energy over the odd-spin sequence in the main band at lower spins, there is no clear pattern in the sideband. Also it should be noted that energy difference between the $S(I_{even})$ and $S(I_{odd})$ curve is consistently somewhat smaller for the sideband than the main band.

4. The B(M1)/B(E2) and B(M1)$_{In}$/B(M1)$_{Out}$ staggering

The experimental reduced transtion probability $B(M1)$ can be a sensitive measure of deviations from axial symme-

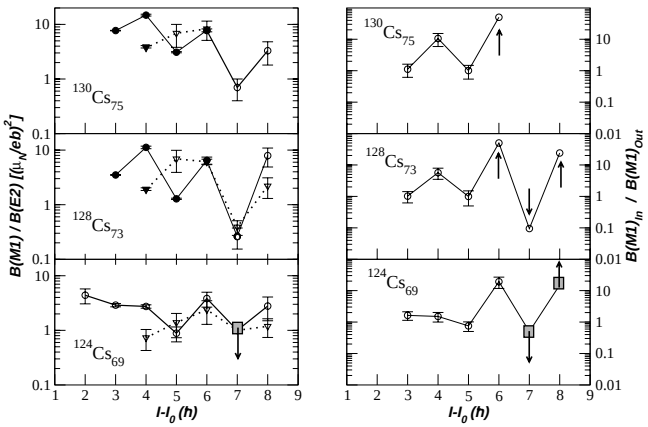

FIG. 16. $B(M1)/B(E2)$ and $B(M1)_{In}/B(M1)_{Out}$ plots for ^{130,128,124}Cs. Closed symbols are ratios obtained from gates set above the level of interest. Open symbols are obtained from the intensities fitted with the ESCL8R package for ^{130,128}Cs, while for ^{124}Cs the intensities listed in Ref. [20] were used with the errors prescribed therein. Points with up (down) arrows represent lower (upper) limits for $B(M1)_{In}/B(M1)_{Out}$ ratios in ^{128,130}Cs when the corresponding $M1$ transitions are too weak to be resolved from background, while the other branching out transitions are observed. Similar points are indicated by shaded squares with pointed arrows for ^{124}Cs, although the upper or lower limits could not be placed from Ref. [20]; these points are included here solely to illustrate the staggering pattern for both ratios. The abscissas show the spin relative to the $I_0=9$ bandhead. Note the different scale of the ordinates between the $B(M1)/B(E2)$ and $B(M1)_{In}/B(M1)_{Out}$ plots. Points connected by solid(dotted) lines are for the main(side) band.

try [27]. Reduced transition probability ratios are experimentally extracted using the relation

$$\frac{B(M1,I\rightarrow I-1)}{B(E2,I\rightarrow I-2)}=0.697\frac{[E_\gamma(I\rightarrow I-2)]^5}{[E_\gamma(I\rightarrow I-1)]^3}\frac{1}{\lambda}\frac{1}{1+\delta^2}\left(\frac{\mu_N^2}{e^2b^2}\right), \tag{7}$$

where λ is the branching ratio obtained from $I_\gamma(I\rightarrow I-2)/I_\gamma(I\rightarrow I-1)$. The mixing ratio terms $\delta^2=I_\gamma[E2(I\rightarrow I-1)]/I_\gamma[M1(I\rightarrow I-1)]$ are neglected since observed values of δ are small and have little effect on the $B(M1)/B(E2)$ ratio compared to the uncertainty in λ. While the $B(M1)/B(E2)$ staggering as a function of spin in the yrast band is clearly present as shown in the left column of Fig. 16, it is not as pronounced in the sideband. Furthermore, the spin dependence of band-member energies for the odd-odd Cs isotopes discussed in the preceeding section is accompanied by a spin dependence for the $B(M1)/B(E2)$ ratios within the yrast band.

Complete information on electromagnetic transitions in regard to the doublet-band structures is important for an understanding of the nuclear shape as well as the behavior of the valence particles. Thus, an investigation of electromagnetic transition properties between the doublet bands will be examined. Ratios between intra-band and interband $B(M1)$ values are obtained experimentally from

$$\frac{B(M1,I^S\rightarrow I^S-1)_{In}}{B(M1,I^S\rightarrow I^S-1)_{Out}}=\left[\frac{E_\gamma(I^S\rightarrow I^S-1)_{Out}}{E_\gamma(I^S\rightarrow I^S-1)_{In}}\right]^3\lambda_{In/Out}\frac{1+\delta_{Out}^2}{1+\delta_{In}^2}, \tag{8}$$

where the branching ratios are defined as $\lambda_{In/Out}=I_\gamma(I^S\rightarrow I^S-1)_{In}/I_\gamma(I^S\rightarrow I^S-1)_{Out}$. The uncertainty in $\lambda_{In/Out}$ makes the contribution of $(1+\delta_{Out}^2)/(1+\delta_{In}^2)$ insignificant, and thus this contribution was not included. The measured values are presented in the right column of Fig. 16. Ratios for ^{124}Cs were reproduced from Ref. [20]. The $B(M1)_{In}/B(M1)_{Out}$ values do exhibit a spin dependence. Furthermore, the $B(M1)_{In}/B(M1)_{Out}$ staggering with spin is in phase with that of the yrast $B(M1)/B(E2)$ ratio staggering, shown on the left column of Fig. 16, revealing a correlation between the two observables. The existence of this doublet-band correlation could represent a sensitive probe into chiral geometries involving triaxial shapes.

B. Two positive-parity sidebands in ^{132}Cs

Unlike the other odd-odd Cs isotopes, the $\pi h_{11/2}\otimes\nu h_{11/2}$ configuration is no longer yrast in ^{132}Cs [17]. Therefore, it is more difficult to observe both the stronger partner and sidebands up to high spin in this nucleus. The sideband labeled $S2$ in Fig. 1 appears to be a better candidate for the chiral partner of the main band Y in terms of degeneracy than the band $S1$ as shown in Fig. 14. However, the I_0+2 and I_0+3 states in the $S2$ band decay to the main band via strong $\Delta I=2$ $E2$ transitions. The sideband observed in the other odd-odd Cs isotopes are linked by intense mixed $\Delta I=1$ $M1/E2$ transitions. The $S2$ band is not likely the partner band despite the fact that the I_0+3 states in the Y and $S2$ bands are only 5 keV apart resulting in cross transitions between the two. A possible configuration assignment for $S2$ is $\pi h_{11/2}\otimes\nu(f_{7/2},h_{9/2})$.

V. THEORETICAL METHODS AND COMPARISON OF THE CALCULATIONS WITH DATA

A. The core-quasiparticle coupling model

In the current studies, a core-quasiparticle coupling model (CQPCM) for odd-odd nuclei, which follows the Kerman-Klein-Dönau-Frauendorf (KKDF) method (for a recent review, see Ref. [28], and references therein), is applied to address the experimental results presented above. This model has a laboratory reference frame basis with the total angular momentum as a good quantum number. Thus, calculated and measured observables are directly related. A corresponding core-particle-hole coupling model without pairing for the valence nucleons has been applied to investigate chiral properties of the $\pi h_{11/2}\otimes\nu h_{11/2}$ doublet bands in odd-odd ^{132}La [9]. In these calculations, pairing for the core nucleons was included in the model for the core, while the valence $h_{11/2}$ proton and neutron were treated as a pure particle and a pure hole, respectively. This simplification worked surprisingly well for ^{132}La mainly due to the fact that for $Z=57$ and N

$=75$ the position of the Fermi level is low and high within the $\pi h_{11/2}$ and $\nu h_{11/2}$ subshells, respectively. The calculations without pairing resulted in doublet $\pi h_{11/2} \otimes \nu h_{11/2}$ structures with theoretical energies and electromagnetic properties in good agreement with those observed experimentally. Scalar operators used to investigate the angular momentum coupling based on the calculated wave functions suggested that the doublets are indeed related to chirality. A model which includes pairing effects for the valence nucleons is necessary, however, to address the current $\pi h_{11/2} \otimes \nu h_{11/2}$ band systematics in the odd-odd $^{124-134}$Cs isotopes, since the range of neutron numbers correspond to a change in the neutron Fermi level from the upper $h_{11/2}$ subshell for $N=79$ to the $h_{11/2}$ midshell for $N=69$. Although, in the current studies, both $h_{11/2}$ valence nucleons are treated as quasiparticles, the valence proton maintains nearly pure particle character due to the Fermi level being low within the $\pi h_{11/2}$ subshell at $Z=55$, while the character of the valence neutron changes from being nearly a pure hole near $N\sim 79$ to having a pronounced quasiparticle character at $N\sim 69$.

The model for a core-quasiparticle coupling for odd-even nuclei which follows the KKDF approach is discussed in a number of papers (see, for example, Refs. [29–31]). In the present studies, the KKDF method is applied to calculate properties of odd-odd nuclei using consecutive odd-particle coupling. In the first step, a proton is coupled to an even-even core, and energies and matrix elements of the electromagnetic operators are calculated for the resulting odd-proton nucleus. This odd-proton nucleus is then treated as a core in an odd-neutron coupling scheme which results in predicted energies and electromagnetic properties for the corresponding odd-odd nucleus. In addition, the neutron can be coupled directly to the even-even core which results in the calculated properties of the corresponding odd-neutron nucleus. Comparisons between calculated and experimental observables for odd-mass nuclei provide a test for the correctness of the coupling scheme as well as the applied model parameters. Since all of the essential model parameters can be fixed from the calculations for odd-mass nuclei, the results for odd-odd nuclei can be considered effectively parameter-free. As pointed out in Ref. [32], for example, Coriolis attenuation is not necessary in this model. A model similar to the one employed here was studied in Ref. [33]; however, it was not applied to a specific nucleus.

Although the details of the model are derived in Refs. [29–31], some of the main features of this derivation are discussed below for completeness and to emphasize its relation to the calculations discussed in Ref. [9]. The presented approach follows that of Ref. [34]. The results of these calculations will then be compared with the experimental data.

1. The Hamiltonian

In the present study, the Hamiltonian consists of a spherically symmetric mean-field, monopole pairing, and separable two-body quadrupole-quadrupole interactions:

$$H=\sum_{\tau,\alpha} \varepsilon_{\tau\alpha}\alpha^{\dagger}_{\tau\alpha}\alpha_{\tau\alpha}-\frac{1}{2}\sum_{\tau} G_{\tau}P^{\dagger}(\tau)P(\tau) -\frac{1}{2}\sum_{\tau,\tau'} \chi_{\tau\tau'}\sum_{m} Q^{\dagger}_{m}(\tau)Q_{m}(\tau'), \tag{9}$$

where $\varepsilon_{\tau\alpha}$ denotes the eigenenergy for the single-particle state $|\alpha\rangle$, which is represented by a set of quantum numbers $(j_{\alpha},m_{\alpha},n_{\alpha},l_{\alpha})$ for the single-particle state $|\alpha\rangle$, and indices $(\tau,\ \tau')$ are running over both protons and neutrons. Two indices $(\tau,\ \tau')$ are required for the two-body quadrupole interaction term, while one index (τ) is sufficient for the pairing since proton-neutron pairing interactions are not considered here.

The separable monopole pairing interactions in Eq. (9) are expressed using the operator $P(\tau)$ which annihilates a pair of protons or neutrons in single-particle states with opposite orientations of angular momentum. This operator is defined as

$$P(\tau)=\sum_{\tau\alpha} \tilde{a}_{\tau\alpha}a_{\tau\alpha}. \tag{10}$$

The symbol $Q(\tau)$ denotes the quadrupole operator for protons or neutrons defined as

$$Q_m(\tau)=\frac{1}{\sqrt{5}}\sum_{\sigma_{\tau\alpha},\sigma_{\tau\alpha'}} q(\sigma_{\tau\alpha},\sigma_{\tau\alpha'})[a^{\dagger}_{\tau\alpha}\tilde{a}_{\tau\alpha'}]_{2m}, \tag{11}$$

where $\sigma_{\tau\alpha}=(j_{\alpha},n_{\alpha},l_{\alpha})$ denotes the set of quantum numbers for the single-particle state $|\alpha\rangle$ without the magnetic quantum number m_{α} for $\tau=\pi$ or $\tau=\nu$. The symbol $q(\sigma_{\tau\alpha},\sigma_{\tau\alpha'})$ denotes the reduced matrix element of the single-particle quadrupole operator calculated between states $|\alpha\rangle$ and $|\alpha'\rangle$. The phase convention for the single-particle wave functions as defined in Sec. 3 A of Ref. [35] is adopted throughout this paper. With this phase convention,

$$Q^{\dagger}_{m}(\tau)=(-)^{m}Q_{-m}(\tau), \tag{12}$$

and the reduced matrix elements

$$q(\sigma_{\tau\alpha},\sigma_{\tau\alpha'})=(-)^{j_{\alpha}-j_{\alpha'}}q(\sigma_{\tau\alpha'},\sigma_{\tau\alpha}) \tag{13}$$

are real. The symbol $[a^{\dagger}_{\tau\alpha}\tilde{a}_{\tau\alpha'}]_{Lm}$ denotes the coupling of spherical tensors, in this case the creation operators for a particle in orbital $|\alpha\rangle$ and a hole in orbital $|\alpha'\rangle$, to a state with angular momentum Lm,

$$[a^{\dagger}_{\tau\alpha}\tilde{a}_{\tau\alpha'}]_{Lm}=\sum_{m_{\alpha},m'_{\alpha}} \langle j_{\alpha}m_{\alpha}j'_{\alpha}m'_{\alpha}|Lm\rangle a^{\dagger}_{\tau\alpha}\tilde{a}_{\tau\alpha'}. \tag{14}$$

2. The basis

There are three natural choices for basis sets which can be constructed for the core-proton-neutron coupling model. In our previous studies in Ref. [9], the basis set was chosen in which the proton and neutron are coupled to a pair with a good angular momentum and then the pair was coupled to an even-even core. The other choice for basis sets is that constructed via the coupling of the valence proton (neutron) to an even-even core and consecutive coupling of the neutron (proton) to the odd-mass core. The basis choice for the current study with a proton coupled to an even-even core and then a neutron coupled to the resulting odd-Z core was made

mainly for convenience in dealing with pairing interactions in this mass region. States with spin IM and additional quantum numbers s resulting from the core-quasiparticle coupling are expanded in this basis which includes $a^{\dagger}_{\tau\mu}|A-1,Rt,r\rangle$ as well as $\tilde{a}_{\tau\mu}|A+1,Rt,r\rangle$ states, where the $|A\pm1,Rt,r\rangle$ are eigenfunctions of the nuclear Hamiltonian for the neighboring core states with angular momentum Rt,[5] and a set of additional quantum numbers labeled r. The expansion coefficients are defined as

$$\langle A,IM,s|a^{\dagger}_{\tau\mu}|A-1,Rt,r\rangle=\langle j_\mu m_\mu Rt|IM\rangle u_{Is(\sigma_{\tau\mu},R,r)},$$

$$\langle A,IM,s|\tilde{a}_{\tau\mu}|A+1,Rt,r\rangle=\langle j_\mu m_\mu Rt|IM\rangle v_{Is(\sigma_{\tau\mu},R,r)}. \tag{15}$$

This expansion, which includes $a^{\dagger}_{\tau\mu}|A-1,Rt,r\rangle$ as well as $\tilde{a}_{\tau\mu}|A+1,Rt,r\rangle$ states, is especially convenient for diagonalization of the Hamiltonian with pairing. However, since the basis is overcomplete,[6] unphysical spurious states are introduced; the identification and elimination of these are discussed below.

3. The Kerman-Klein-Dönau-Frauendorf method for core-quasiparticle coupling

The Heisenberg equations of motion for fermion creation and annihilation operators for the Hamiltonian with pairing are analogous to those derived in Ref. [9] for a core-particle or core-hole coupling model:

$$\begin{aligned}[H,a^{\dagger}_{\tau\mu}]=&(\varepsilon_{\tau\mu}-G_\tau)a^{\dagger}_{\tau\mu}-G_\tau\tilde{a}_{\tau\mu}P^{\dagger}(\tau)\\&-\sum_{\tau'}\chi_{\tau\tau'}\sum_{\sigma_{\tau\mu'}}\frac{1}{\sqrt{2j_\mu+1}}q(\sigma_{\tau\mu},\sigma_{\tau\mu'})\\&\times[a^{\dagger}_{\tau\mu'}Q(\tau')]_{j_\mu m_\mu}\\&-\frac{1}{2}\chi_{\tau\tau}\sum_{\mu'}\sum_{\sigma_{\tau\alpha}}\frac{1}{2j_\mu+1}q(\sigma_{\tau\mu},\sigma_{\tau\alpha})\\&\times q(\sigma_{\tau\mu'},\sigma_{\tau\alpha})a^{\dagger}_{\tau\mu'}\delta_{j_\mu j_{\mu'}}\delta_{m_\mu m_{\mu'}},\end{aligned}$$

$$\begin{aligned}[H,\tilde{a}_{\tau\mu}]=&-\varepsilon_{\tau\mu}\tilde{a}_{\tau\mu}-G_\tau a^{\dagger}_{\tau\mu}P(\tau)\\&+\sum_{\tau'}\chi_{\tau\tau'}\sum_{\sigma_{\tau\mu'}}\frac{1}{\sqrt{2j_\mu+1}}q(\sigma_{\tau\mu},\sigma_{\tau\mu'})\\&\times q(\sigma_{\tau\mu'},\sigma_{\tau\alpha})\tilde{a}_{\tau\mu'}\delta_{j_\mu j_{\mu'}}\delta_{m_\mu m_{\mu'}}\\&-\frac{1}{2}\chi_{\tau\tau}\sum_{\mu'}\sum_{\sigma_{\tau\alpha}}\frac{1}{2j_\mu+1}q(\sigma_{\tau\mu},\sigma_{\tau\alpha})\\&\times q(\sigma_{\tau\mu'},\sigma_{\tau\alpha})\tilde{a}_{\tau\mu'}\delta_{j_\mu j_{\mu'}}\delta_{m_\mu m_{\mu'}}.\end{aligned} \tag{16}$$

When wave functions for the core and those wave functions defined in the preceding section for the nucleon coupling are applied to the right-hand and the left-hand side of the above equations, the following is derived for the expansion coefficients:

$$\begin{aligned}&E_{Is(\sigma_{\tau\mu},R,r)}u_{Is(\sigma_{\tau\mu},R,r)}\\&\quad=v_{Is(\sigma_{\tau\mu},R,r)}\Delta+\sum_{\sigma_{\tau\mu'},R',r'}H^{p}_{(\sigma_{\tau\mu},R,r)(\sigma_{\tau\mu'},R',r')}\\&\qquad\times u_{Is(\sigma_{\tau\mu'},R',r')},\\&E_{Is(\sigma_{\tau\mu},R,r)}v_{Is(\sigma_{\tau\mu},R,r)}\\&\quad=u_{Is(\sigma_{\tau\mu},R,r)}\Delta+\sum_{\sigma_{\tau\mu'},R',r'}H^{h}_{(\sigma_{\tau\mu},R,r)(\sigma_{\tau\mu'},R',r')}\\&\qquad\times v_{Is(\sigma_{\tau\mu'},R',r')},\end{aligned} \tag{17}$$

under the assumption that the matrix element of the pair transfer operator between $A\pm1$ core states is

$$\langle A-1,R't',r'|G_\tau P(\tau)|A+1,Rt,r\rangle=\delta_{RtR't'}\delta_{rr'}\Delta. \tag{18}$$

The matrix elements of H^p and H^h are given by

$$\begin{aligned}H^{p}_{(\sigma_{\tau\mu},R,r)(\sigma_{\tau\mu'},R',r')}=&[E^{A-1}_{Rr}+(\varepsilon_{\tau\mu}-\lambda_F)]\delta_{\sigma_{\tau\mu}\sigma_{\tau\mu'}}\delta_{RR'}\delta_{rr'}\\&-\chi(-)^{j_{\mu'}+R+I}\begin{Bmatrix}j_{\mu'}&2&j_\mu\\R&I&R'\end{Bmatrix}\\&\times q(\sigma_{\tau\mu},\sigma_{\tau\mu'})q^{A-1}(R,r,R',r'),\\H^{h}_{(\sigma_{\tau\mu},R,r)(\sigma_{\tau\mu'},R',r')}=&[E^{A+1}_{Rr}-(\varepsilon_{\tau\mu}-\lambda_F)]\delta_{\sigma_{\tau\mu}\sigma_{\tau\mu'}}\delta_{RR'}\delta_{rr'}\\&+\chi(-)^{j_{\mu'}+R+I}\begin{Bmatrix}j_{\mu'}&2&j_\mu\\R&I&R'\end{Bmatrix}\\&\times q(\sigma_{\tau\mu},\sigma_{\tau\mu'})q^{A+1}(R,r,R',r').\end{aligned} \tag{19}$$

TABLE XII. Four core parameters fitted from experimental values of ^{128}Xe [38,42].

J_{00}	1.975 ($\hbar^2$/MeV)
C	4.43×10^{-3} (MeV$^3/\hbar^4$)
β	0.19
γ	27°

[5] Rt denotes two quantum numbers R and t, which are the core angular momentum and its projection, respectively. This is analogous to the IM notation.

[6] In principle, a basis which consists of $a^{\dagger}_{\tau\mu}|A-1,Rt,r\rangle$ or $\tilde{a}_{\tau\mu}|A+1,Rt,r\rangle$ states only should be sufficient to expand the wave function of interest.

In the equations above, E_{Is} denotes the energy of the state with quantum numbers Is resulting from the nucleon coupling. For the core states with quantum numbers (R,r), the excitation energy of a state with respect to the ground state is denoted by $E_{Rr}^{A\pm1}$. The parameter λ_F, defined by the energy difference of the core ground states

$$\lambda_F=\frac{1}{2}[E_0(A+1)-E_0(A-1)]+\frac{1}{2}G_\tau, \tag{20}$$

is related to the Fermi energy for the nucleons being coupled by

$$E_F=E_0(A\mp1)\pm\lambda_F. \tag{21}$$

In the discussion below, λ_F is treated as a parameter of the model. The reduced matrix elements of the quadrupole operator between core states with quantum numbers (R,r) and (R',r') are denoted by $q^{A\pm1}(R,r,R',r')$. Equations (19) were derived under the assumption $\chi_{\pi\pi}=\chi_{\nu\nu}=\chi_{\pi\nu}=\chi$. The single-particle valence space for the current calculation is restricted to the $h_{11/2}$ orbital; in such an approximation, the last terms on the right-hand sides of Eq. (16) can be neglected since they result only in an additive constant to the diagonal matrix elements of H^p and H^h.

Equations (17) define an eigenvalue problem

$$E_{Is}\begin{pmatrix}u\\v\end{pmatrix}=H\begin{pmatrix}u\\v\end{pmatrix},\quad H=\begin{pmatrix}H^p & \Delta\\ \Delta & H^h\end{pmatrix}, \tag{22}$$

which is solved below yielding energies and wave functions for states resulting from the nucleon coupling.

4. Diagonalization of the Hamiltonian and elimination of spurious states

As pointed out in the basis discussion (Sec. V A 2), overcompleteness of the model basis results in unphysical spurious states which need to be eliminated during the diagonalization of Eq. (22). The diagonalization is carried out, therefore, in two steps following the method of Refs. [29,31,34].

The Hamiltonian given by Eq. (22) can be represented as the sum of two parts $H=H_a+H_s$ with

$$H_a=\begin{pmatrix}\frac{1}{2}(H^p-H^h) & \Delta\\ \Delta & -\frac{1}{2}(H^p-H^h)\end{pmatrix},$$

$$H_s=\begin{pmatrix}\frac{1}{2}(H^p+H^h) & 0\\ 0 & \frac{1}{2}(H^p+H^h)\end{pmatrix}. \tag{23}$$

As the first step, the matrix H_a is diagonalized. This is done by the diagonalization of the $\frac{1}{2}(H^p-H^h)$ matrix (which yields effective single-particle energies for the qQ coupling) followed by a subsequent quasiparticle transformation which diagonalizes the H_a matrix and defines quasiparticle energies and wave functions. Because of the structure of the H_a matrix, each quasiparticle state with energy $\bar{\varepsilon}$ and wave function $(\bar{u},\bar{v})$ has a partner state with energy $-\bar{\varepsilon}$ and wave functions $(-\bar{v},\bar{u})$. Quasiparticle states with positive energies only are used for the diagonalization of the $\frac{1}{2}(H^p+H^h)$ matrix in the second step, while quasiparticles with negative energies are treated as spurious states. Diagonalization of the $\frac{1}{2}(H^p+H^h)$ matrix in a positive-energy quasiparticle basis yields the energies E_{Is} and wave function (u,v) for states resulting from the nucleon coupling.

It should be noted that, in the case of the present studies, the elimination of the proton spurious states is of relatively little importance compared to the elimination of the neutron spurious states. This is due to the fact that the proton Fermi energy λ_F^π is low compared to the energy of the spherical $\pi h_{11/2}$ state of interest and the wave function for an odd-Z nucleus is dominated by the $a^\dagger_{\pi h_{11/2}}|A-1,Rt,r\rangle$ components.

5. Electromagnetic properties

The expansion coefficients resulting from the above diagonalization are used to compute the reduced matrix elements of the $M1$ and $E2$ operators. The reduced matrix element of the operator $\mathcal{M}(\Lambda)$ is given by

$$\begin{aligned}\langle A,I's'||\mathcal{M}(\Lambda)||A,Is\rangle=\sqrt{2I+1}\sqrt{2I'+1}\Bigg\{&\sum_{\sigma_{\tau\mu}}\sum_{R,r,R',r'}\Bigg((-)^{j_\mu+R+I'+\Lambda}\begin{Bmatrix}I' & \Lambda & I\\ R & j_\mu & R'\end{Bmatrix}\\ &\times[\langle A-1,R',r'||\mathcal{M}(\Lambda)||A-1,R,r\rangle u_{Is(\sigma_{\tau\mu},R,r)}u_{I's'(\sigma_{\tau\mu},R',r')}+\langle A+1,R',r'||\mathcal{M}(\Lambda)\\ &\times||A+1,R,r\rangle v_{Is(\sigma_{\tau\mu},R,r)}v_{I's'(\sigma_{\tau\mu},R',r')}]\Bigg)+\sum_{\sigma_{\tau\mu},\sigma_{\tau\mu'}}\sum_{R,r}\Bigg((-)^{j_{\mu'}+R+I+\Lambda}\begin{Bmatrix}I' & \Lambda & I\\ j_\mu & R & j_{\mu'}\end{Bmatrix}\\ &\times\langle\sigma_{\tau\mu'}||\mathcal{M}(\Lambda)||\sigma_{\tau\mu}\rangle[u_{Is(\sigma_{\tau\mu},R,r)}u_{I's'(\sigma_{\tau\mu'},R,r)}+cv_{Is(\sigma_{\tau\mu},R,r)}v_{I's'(\sigma_{\tau\mu'},R,r)}]\Bigg)\Bigg\},\end{aligned} \tag{24}$$

FIG. 17. Comparison of energy levels between the calculation and the experiment for ^{128}Xe. Experimental data are from Ref. [38].

where

$$c = \begin{cases} -1 & \text{for electric multipoles} \\ +1 & \text{for magnetic multipoles,} \end{cases} \tag{25}$$

is a factor related to the transformation properties of the matrix element of the $\mathcal{M}(\Lambda)$ operator under particle-hole conjugation as discussed in Sec. 3.1 b of Ref. [35].

B. Application of the model to ^{128}Cs

1. A rigid triaxial core: ^{128}Xe

The rigid triaxial rotor of Davydov and Filippov [36] is employed for modeling the core. The Hamiltonian of the rotor is defined as

$$H_{rot} = \sum_{k=1}^{3} \frac{R_k^2}{2J_k}, \tag{26}$$

where R_k and J_k are the component of the total angular momentum of the core and the moment of inertia along the principal axis k, respectively. Although the shape of the rotor is assumed to be rigid, its moment of inertia is of a different character. In fact, variable irrotational-flow moments of inertia are used as given by

$$J_{kR} = \frac{4}{3} J_{0R} \sin^2\left(\gamma - \frac{2k\pi}{3}\right), \quad k = 1,2,3. \tag{27}$$

The spin-dependent moment of inertia J_{0R} is a unique positive solution of Eqs. (28) and (29) as described by Mariscotti *et al.* [37]:

$$E_R(J_{0R}) = \frac{1}{2} C (J_{0R} - J_{00})^2 + \frac{1}{2} \frac{R(R+1)}{J_{0R}}, \tag{28}$$

$$\frac{\partial E(J_{0R})}{\partial J_{0R}} = 0, \tag{29}$$

where E_R represents energies in the ground-state band of the even-even core, and J_{00} and C are fitted from the experimental E_R [38]. Similar methods for simulating cores are applied in the triaxial rotor plus particle description of negative-parity states in odd-A ^{123,125}Xe [39,40] and ^{125,127,129}Cs [41].

In addition to J_{00} and C, the deformation parameters β and γ are fitted from the experimental $B(E2;2^+ \to 0^+) = 0.15(8)$ (e^2b^2) [42] and the energy ratio of the first and the second 2^+ state [36], respectively. The core parameters are summarized in Table XII. Figure 17 shows the fitted energy levels together with those from the experiment [38]. The yrast band fits remarkably well. The calculated energy levels for the γ band are noticeably overestimated for states with spins higher than three, reflecting the fact that γ softness is required to fit the data properly.

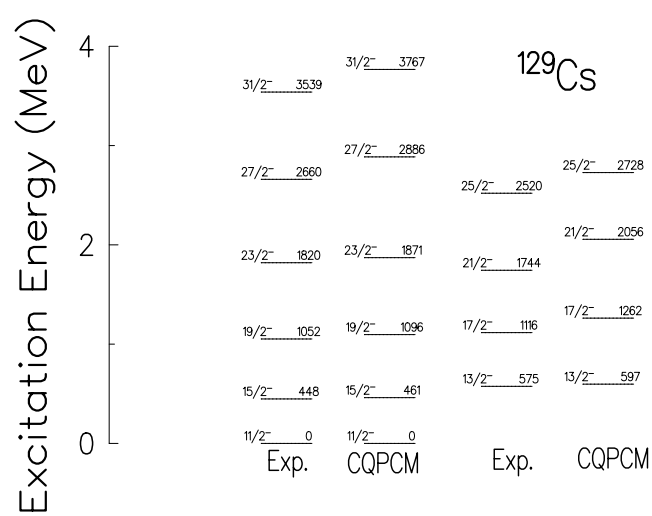

FIG. 18. Comparison of energy levels between the calculation and the experiment for ^{129}Cs. Experimental data are from Ref. [43].

TABLE XIII. Quadrupole-quadrupole coupling constant and relative Fermi levels for protons and neutrons for ^{128}Cs.

χ	10 (MeV/b^2)
λ_π-$\varepsilon_{h_{11/2}}$	-2.5 MeV
λ_ν-$\varepsilon_{h_{11/2}}$	$+1.75$ MeV

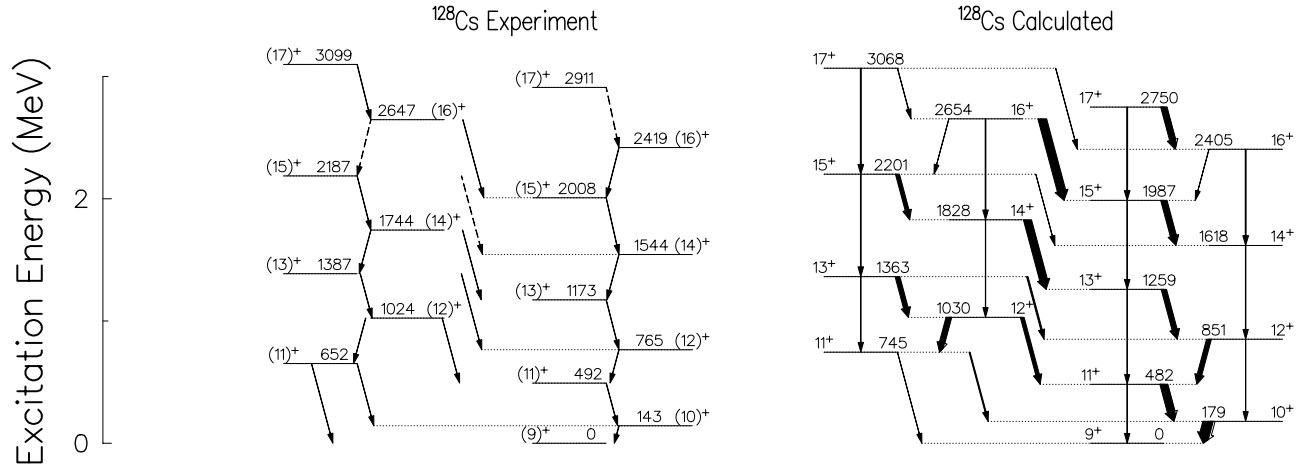

FIG. 19. On the right: a level scheme predicted for ^{128}Cs using the model with parameters listed in Tables XII and XIII. Widths of arrows are proportional to calculated reduced transition probabilities, namely, $B(M1)$ and $B(E2)$. On the left: The level scheme obtained from the current study. The arrow width is constant. The broken arrows represent unobserved transitions. A bandhead $I_0^\pi = 9^+$ is assumed.

2. The consecutive CQPCM: odd-odd ^{128}Cs

Using the KKDF method, the valence $h_{11/2}$ proton is coupled to the calculated even-even ^{128}Xe core described in the preceding section yielding results for ^{129}Cs. Good agreement between the calculated and the experimental energy levels [43] for the $\pi h_{11/2}$ band is obtained with the coupling constant $\chi = 10$ MeV/b^2 and $\lambda_\pi - \varepsilon_{h_{11/2}} = -2.5$ MeV, where λ_π is the Fermi level for proton and $\varepsilon_{h_{11/2}}$ is the energy for the $h_{11/2}$ spherical orbit. The calculated energy levels are shown in Fig. 18 and the two parameters are listed in Table XIII. Subsequently, the same method is reapplied by coupling the valence $h_{11/2}$ neutron to the calculated ^{129}Cs core, yielding the odd-odd ^{128}Cs results.

The calculated and experimental energy levels for ^{128}Cs are compared in Fig. 19 for the neutron Fermi level $\lambda_\nu - \varepsilon_{h_{11/2}} = +1.75$ MeV. Nearly degenerate $\pi h_{11/2} \otimes \nu h_{11/2}$ doublet bands emerge for a range of neutron Fermi levels in the model calculations. The predicted energy levels plotted as a function of spin in Fig. 20 show that not only the overall excitation energy, but also the energy difference between the ground and first excited band are sensitive to the neutron Fermi level. The experimental data are best reproduced when the neutron Fermi level measured relative to the spherical $h_{11/2}$ shell is at $\lambda_\nu - \varepsilon_{h_{11/2}} = +1.75$ MeV as shown in the

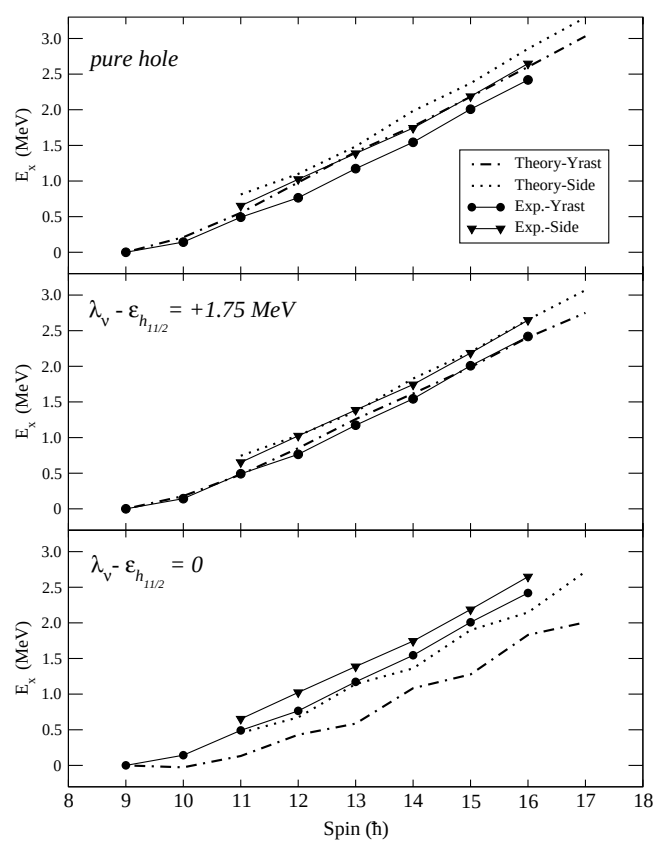

FIG. 20. Calculated excitation energies in ^{128}Cs as a function of spin I with different relative neutron Fermi levels (dot-dashed lines for the yrast and dotted lines for the sideband). The experimental curves are indicated by filled symbols with solid lines.

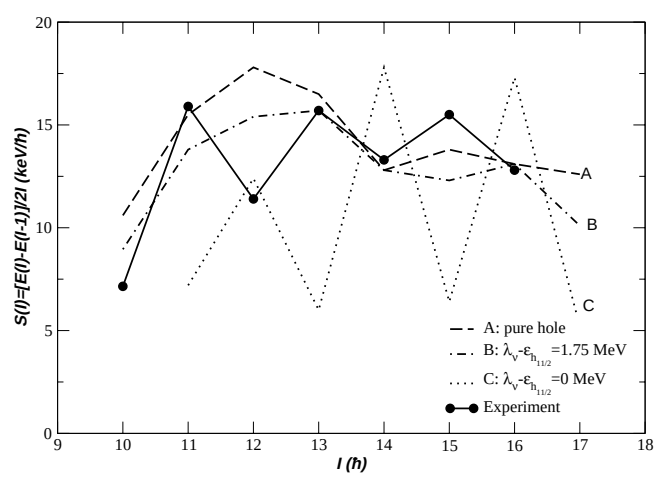

FIG. 21. Calculated $S(I)$ values (broken lines) for the yrast band in ^{128}Cs, with different relative neutron Fermi levels. The experimental values are filled circles connected by solid lines.

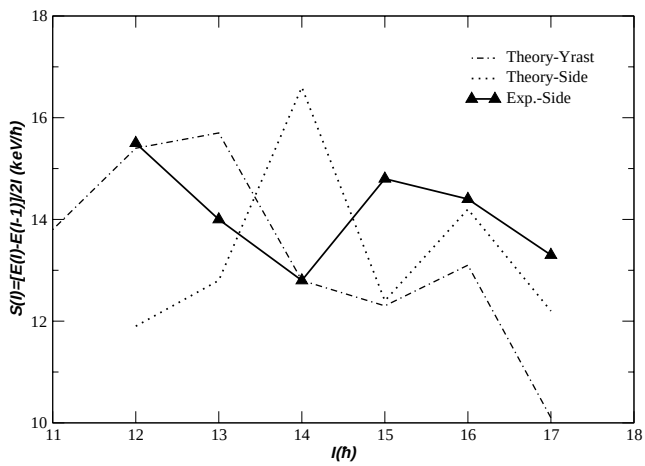

FIG. 22. The $S(I)$ values calculated for the parameters listed in Tables XII and XIII for the sidebands and yrast bands in ^{128}Cs (broken lines). Experimental points for the sideband are connected by solid lines.

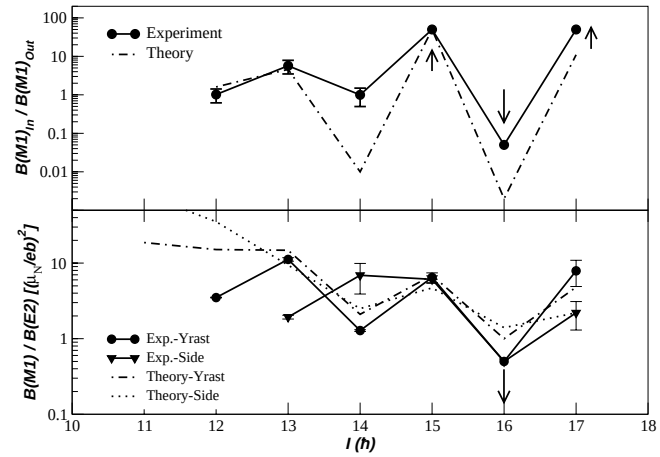

FIG. 23. Top: Calculated (dot-dashed line) and experimental (solid line) values for $B(M1)_{In}/B(M1)_{Out}$ in ^{128}Cs. For data points with an arrow refer to Fig. 16. Bottom: Comparisons between the calculations and data in $B(M1)/B(E2)$ values for both the yrast and sideband in ^{128}Cs.

middle panel of Fig. 20. When the relative Fermi level is at zero ($\lambda_\nu = \varepsilon_{h_{11/2}}$), resulting in equal amplitudes of particle-like and holelike states for the quasiparticle wave function, the energy difference between the two bands is excessively large and the model under-predicts the energy E vs spin I curves (bottom panel). On the other hand, when a pure neutron hole is considered, the model over-predicts the E vs I curves and near degenerate states result at spin 13^+ (top panel). Provided that the γ and β values are fixed, the above trend is expected within the chiral interpretation; as the Fermi level increases, the high-j quasihole couples more strongly to the long axis of the triaxial core resulting in a good chiral geometry.

One important point to note, as discussed in Ref. [9], however, is that larger β values for $\gamma \sim 30°$ have an effect of strengthening the coupling of the valence particle to the core. This effect contributes to the stabilization of the chiral geometry. By the same argument, reduced β deformations, as occur when the neutron number approaches the magic number $N=82$, destabilize the perpendicular coupling of angular momenta. The neutron Fermi level situated in the $h_{11/2}$ midshell influences both the β and γ value of the triaxial core. The energy differences between the partner bands in ^{124,126}Cs are comparable to those in ^{128}Cs. This suggests that the chiral conditions do not change rapidly with decreasing neutron number in these isotopes since the enhanced stability due to the increased β compensates the less-perpendicular coupling of the single-particle angular momenta for quasineutrons near the midshell as compared to ^{128}Cs. The observation of chiral doublet bands in the $A \sim 130$ region indicates, therefore, that optimal chiral conditions realized in ^{134}Pr are surrounded by a soft chiral-geometry region which extend to the low-N Cs isotopes.

The position of the Fermi level has an influence on the energy splitting pattern, as well, within the ground-state $\pi h_{11/2} \otimes \nu h_{11/2}$ band as shown in Fig. 21. For $\lambda_\nu = \varepsilon_{h_{11/2}}$ (C), the calculated staggering pattern is opposite to that observed above spin 12, i.e., odd-spin states lie lower in energy. At λ_ν-$\varepsilon_{h_{11/2}} = +1.75$ MeV (B), the staggering pattern begins to be restored, and for a pure hole (A), the even-spin states are clearly favored in energy in the calculation above spin 12. In all cases, the model fails to reproduce the experimental results at spin 12. The cause of this deviation at this particular spin is not understood. However, at lower spin, proton-neutron (pn) residual interactions are expected to play an important part in causing the odd-/even-spin dependence of $S(I)$ [26]. These residual interactions might also enhance the overall staggering amplitude, which could explain the under-estimated values of the amplitude predicted by the model.

TABLE XIV. Calculated reduced transition probabilities for ^{128}Cs.

I	$B(E2;I\to I-2)$ (e^2b^2)		$B(M1;I\to I-1)$ (μ_N^2)		$B(M1;I^S\to I^S-1)$ (μ_N^2)
	Yrast	Side	Yrast	Side$=B(M1)_{In}$	Side$=B(M1)_{Out}$
17	0.244	0.244	1.62	0.605	0.075
16	0.230	0.184	0.034	0.032	2.31
15	0.177	0.187	1.64	1.04	0.050
14	0.125	0.088	0.00	0.00	2.13
13	0.079	0.118	1.39	1.23	0.386
12	0.062	0.034	1.25	1.43	1.00

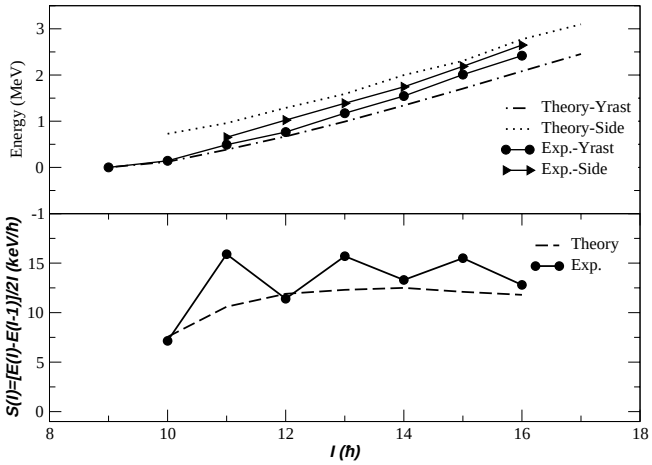

FIG. 24. Calculations for ^{128}Cs assuming $\gamma=0°$(axially symmetric core). The top panel shows the excitation energy as a function of spin, and $S(I)$ is shown in the bottom panel.

Since the present study does not include the pn interactions, their effect on the discussed observables is not addressed in this paper. The better agreement at higher spin could be due to the fact that the assumed rigid triaxial core is more applicable than in the lower-spin range since the γ-soft core will be driven towards $\gamma=30°$ by the increasing core rotation which minimizes the rotational energy. It is argued in Ref. [44] that the energy splitting is a very sensitive probe of shape changes in nuclei. Thus, γ-soft cores as well as the inclusion of pn interactions are additional areas for theoretical investigations. (Interestingly, the calculation for λ_ν-$\varepsilon_{h_{11/2}}=+1.75$ MeV predicts that the odd-spin states are apparently favored in energy for the sideband as shown in Fig. 22, while the data do not show a clear spin dependence.)

The model with the parameters listed in Tables XII and XIII correctly predicts the staggering pattern of $B(M1)/B(E2)$ in the yrast band and $B(M1)_{In}/B(M1)_{Out}$ for the sideband as presented in the lower and upper panels of Fig. 23, respectively. Calculated reduced electromagnetic transition probabilities are tabulated in Table XIV. While the $B(E2)$ increases somewhat smoothly with spin, the $B(M1)$ as well as $B(M1)_{Out}$ values depend markedly on the odd/even-ness of the spin. $B(M1;I_{odd}\rightarrow(I-1)_{even})$ and $B(M1;I^S_{even}\rightarrow(I^S-1)_{odd})_{Out}$ are in many cases two orders of magnitude larger than $B(M1;I_{even}\rightarrow(I-1)_{odd})$ and $B(M1;I^S_{odd}\rightarrow(I^S-1)_{even})_{Out}$, respectively; thus, according to the model, staggering of the ratios for the electromagnetic transitions is attributed to the spin dependence of the $B(M1)$ values. Notably, another consequence of the above is the much larger staggering amplitude for the $B(M1)_{In}/B(M1)_{Out}$ than the $B(M1)/B(E2)$ ratios.

Since the core energies and electromagnetic properties must be externally provided, the current theoretical approach allows various assumptions for the core to be tested against measurement. The assumed stable triaxial deformation and irrotational-flow moment of inertia imposed on the core are shown to be appropriate in ^{128}Cs. When γ is changed from 27° to 0° (axially symmetric core) keeping the remaining parameters the same, drastic changes are made to all of the observables discussed in the paper. The sideband is displaced to higher energy by more than a factor of 2 compared with the data, as shown in the upper panel of Fig. 24. The spin dependence of $S(I)$ is lost, and $S(I)$ becomes more or less constant over a large interval of spin, as presented in the lower panel of Fig. 24. Similarly, the $B(M1)$ decreases smoothly, and the $B(E2)$ steadily increases as a function of spin (see inset in Fig. 25.) As a result, the staggering in the $B(M1)/B(E2)$ ratio is not seen with an axially symmetric core, as shown in Fig. 25.

It is very encouraging that the present model, with rather crude approximations of the core, successfully reproduces experimental features related to the doublet bands described in this paper. Once the odd-A core is determined, only the neutron Fermi level is an adjustable parameter for the fit to the data. Considering the Fermi level fits of the valence proton and neutron, the chiral interpretation of the doublet bands built on the high-j $\pi h_{11/2}\otimes\nu h_{11/2}$ configuration is supported. Further analysis including the calculation of the coupling

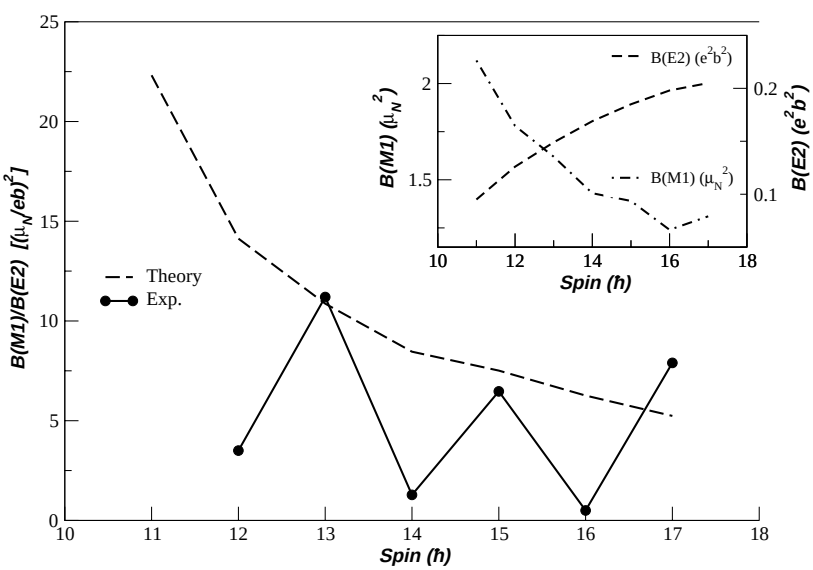

FIG. 25. The calculated $B(M1)/B(E2)$ values (dashed lines) assuming $\gamma=0°$ for ^{128}Cs compared with the corresponding data (solid lines). The inset shows the calculated absolute $B(M1)$ and $B(E2)$ values as a function of spin.

angles, namely, $\langle \mathbf{R} \cdot \mathbf{j}_{\pi(\nu)} \rangle$ and $\langle \mathbf{j}_\pi \cdot \mathbf{j}_\nu \rangle$ as well as orientation operator $\sigma = (\mathbf{j}_\pi \times \mathbf{j}_\nu) \cdot \mathbf{R}$ are planned. A formalism equivalent to that applied in Ref. [9] would need to be developed for the current basis.

VI. CONCLUSIONS

The odd-odd $^{128-134}$Cs isotopes have been studied in the present work as a search for chiral doublet bands. New γ rays were identified in ^{134}Cs; however, the nucleus did not show significant collectivity. Sidebands to the $\pi h_{11/2} \otimes \nu h_{11/2}$ yrast partner band were identified in the ^{128,130,132}Cs isotopes in the current study. Positive parity and relative spins of these sidebands were deduced based on the mixed $\Delta I = 1$ $M1/E2$ character of the linking transitions between the two bands, which is uniquely determined from DCO analyses. This results in near degenerate $\Delta I = 1$ bands as expected when a chiral geometry is attained in these nuclei. Smooth variation of the excitation energy for the sidebands from ^{124}Cs to ^{132}Cs provides further support to the energy systematics proposed in Ref. [8] for odd-odd Cs isotopes. These experimental data make the chain of odd-odd Cs nuclei a reliable source of information on properties such as the odd-/even-spin dependence of $S(I)$ values in the mass 130 region and the staggering of $B(M1)/B(E2)$ values in the yrast partner bands. Combined with the sidebands, the staggering of $B(M1)_{In}/B(M1)_{Out}$ correlated with that of $B(M1)/B(E2)$ was experimentally recognized. The core-quasiparticle coupling model, following the Kerman-Klein-Dönau-Frauendorf method, was applied in order to investigate chirality in ^{128}Cs. With this model an explicit assumption of a triaxial rigid core with an irrotational-flow moment of inertia was tested by comparing the calculations to the experimental result.

A good overall agreement between the calculations and the experiment for the various observables was remarkable considering the simplifications made. Therefore, the present study suggests that indeed triaxiality is an essential feature in understanding the underlying physics in odd-odd Cs isotopes and perhaps neighboring transitional nuclei in this mass region. As a consequence of a stable triaxial deformation, i.e., a substantial deviation from axial symmetry, a proper language to describe physical phenomena related to triaxiality is required. In particular, what is referred to as signature inversion for the $A \sim 130$ region has a different origin than in axially deformed regions. Classification of excited states into rotational bands according to the signature quantum number is suitable and successful in nuclei in which the total angular momentum coincides with a principal axis; however, this scheme is not appropriate if applied in triaxial odd-odd nuclei when the total angular momentum does not coincide with any principal axes. Hence the word *signature* becomes misleading when used in this case.

Further investigations are necessary to study the influence of triaxiality in this mass region. The theoretical method employed in the current study for ^{128}Cs can be equally applied to the lighter Cs isotopes, where chiral geometries are not expected, in order to investigate the sensitivity of $S(I)$ and $B(M1)$ values to triaxiality.

ACKNOWLEDGMENTS

Authors would like to thank Dr. A. Klein, Dr. Ch. Droste, and Dr. T. Saitoh for careful reading of the manuscript and valuable comments.

[1] K. Starosta *et al.*, Phys. Rev. Lett. **86**, 971 (2001).
[2] A.A. Hecht *et al.*, Phys. Rev. C **63**, 051302(R) (2001).
[3] T. Koike, K. Starosta, C.J. Chiara, D.B. Fossan, and D.R. LaFosse, Phys. Rev. C **63**, 061304(R) (2001).
[4] D.J. Hartley *et al.*, Phys. Rev. C **64**, 031304(R) (2001).
[5] R.A. Bark, A.M. Baxter, A.P. Byrne, G.D. Dracoulis, T. Kibédi, T.R. McGoram, and S.M. Mullins, Nucl. Phys. **A691**, 577 (2001).
[6] C.M. Petrache, G. de Angelis, D. Bucurescu, M. Ivascu, D. Bazzacco, and S. Lunardi, Z. Phys. A **344**, 227 (1992); C.M. Petrache *et al.*, Nucl. Phys. **A597**, 106 (1996).
[7] S. Frauendorf and J. Meng, Nucl. Phys. **A617**, 131 (1997).
[8] Y. Liu, J. Lu, Y. Ma, S. Zhou, and H. Zheng, Phys. Rev. C **54**, 719 (1996); **58**, 1849 (1998).
[9] K. Starosta, C.J. Chiara, D.B. Fossan, T. Koike, T.T.S. Kuo, D.R. LaFosse, S.G. Rohoziński, Ch. Droste, T. Morek, and J. Srebrny, Phys. Rev. C **65**, 044328 (2002).
[10] V.I. Dimitrov, S. Frauendorf, and F. Dönau, Phys. Rev. Lett. **84**, 5732 (2000).
[11] H. Madokoro (private communication).
[12] D.C. Radford, Nucl. Instrum. Methods Phys. Res. A **361**, 297 (1995); **361**, 306 (1995).
[13] A. Krämer-Flecken, T. Morek, R.M. Lieder, W. Gast, G. Hebbinghaus, H.M. Jeger, and W. Urban, Nucl. Instrum. Methods Phys. Res. A **275**, 333 (1989); K.S. Krane, R.M. Steffen, and R.M. Wheeler, Nucl. Data Tables A **11**, 351 (1973).
[14] E.S. Paul *et al.*, Phys. Rev. C **40**, 619 (1989).
[15] P.R. Sala, N. Blasi, G. Lo Bianco, A. Mazzoleni, R. Reinhardt, K. Schiffer, K.P. Schmittgen, G. Siems, and P. von Brentano, Nucl. Phys. **A531**, 383 (1991).
[16] R. Kumar, D. Mehta, N. Singh, H. Kaur, A. Görgen, S. Chmel, R.P. Singh, and S. Murlithar, Eur. Phys. J. A **11**, 5 (2001).
[17] T. Hayakawa, J. Lu, K. Furutaka, T. Komatsubara, T. Shizuma, N. Hashimoto, T. Saitoh, M. Kidera, Y. Hatsukawa, and M. Oshima, Z. Phys. A **357**, 349 (1997).
[18] M. Bogdanović *et al.*, Nucl. Phys. **A470**, 13 (1987).
[19] T. Komatsubara *et al.*, Nucl. Phys. **A557**, 419c (1993).
[20] A. Gizon *et al.*, Nucl. Phys. **A694**, 63 (2001).
[21] C.-B. Moon, S.J. Chae, J.H. Ha, T. Komatsubara, Y. Sasaki, T. Jumatsu, K. Yamada, K. Satou, and K. Furuno, Nucl. Phys. **A696**, 45 (2001).
[22] C.-B. Moon, T. Komatsubara, and K. Furuno, Nucl. Phys. **A674**, 343 (2000); **A678**, 457 (2000).
[23] Stefan Frauendorf, Rev. Mod. Phys. **73**, 463 (2001).
[24] K. Starosta, T. Koike, C.J. Chiara, D.B. Fossan, and D.R. LaFosse, Nucl. Phys. **A682**, 375c (2001).

[25] L.L. Riedinger *et al.*, Acta Phys. Pol. B **32**, 2613 (2001).
[26] N. Tajima, Nucl. Phys. **A572**, 365 (1994).
[27] I. Hamamoto and B. Mottelson, Phys. Lett. **167B**, 370 (1986).
[28] A. Klein, Phys. Rev. C **63**, 014316 (2000).
[29] F. Dönau and S. Frauendorf, Phys. Lett. **71B**, 263 (1977).
[30] Ch. Droste, D. Chlebowska, J. Dobaczewski, F. Dönau, A. Kerek, G. Leander, J. Srebrny, and W. Waluś, Nucl. Phys. **A341**, 98 (1980).
[31] F. Dönau and U. Hagemann, Z. Phys. A **293**, 31 (1979).
[32] P. Protopapas and A. Klein, Phys. Rev. C **55**, 1810 (1996).
[33] F. Dönau, in *Microscopic Approaches to Nuclear Structure Calculations*, edited by A. Covello (Societa Italiana di Fisica, Sorrento, 1986); (private communication).
[34] P. Brewczyk, M.Sc. thesis, Institute of Theoretical Physics, Warsaw University.
[35] A. Bohr and B. Mottelson, *Nuclear Structure* (Benjamin, New York, 1975).
[36] A.S. Davydov and C.F. Filippov, Nucl. Phys. **B8**, 237 (1958).
[37] M.A. Mariscotti, G. Scharff-Goldhaber, and B. Buck, Phys. Rev. **178**, 1864 (1969).
[38] U. Neuneyer, A. Mertens, R. Kühn, I. Wiedenhöver, O. Vogel, M. Wilhellm, M. Luig, K.O. Zell, A. Gelberg, P. von Brentano, and T. Otsuka, Nucl. Phys. **A607**, 299 (1996).
[39] A. Gade, H. Meise, I. Wiedenhöver, A. Schmidt, A. Gelberg, and P. von Brentano, Nucl. Phys. **A686**, 3 (2001).
[40] D. Lieberz, A. Gelberg, A. Grandearth, P. von Brentano, I. Ragnarsson, and P.B. Semmes, Nucl. Phys. **A529**, 1 (1991).
[41] O. Vogel, A. Gelberg, R.V. Jolos, and P. von Brentano, Nucl. Phys. **A576**, 109 (1994).
[42] I. Wiedenhöver, A. Gelberg, T. Otsuka, N. Pietralla, J. Gableske, A. Dewald, and P. von Brentano, Phys. Rev. C **56**, R2354 (1997).
[43] L. Hildingsson, W. Klamra, Th. Lindblad, F. Liden, Y. Liang, R. Ma, E.S. Paul, N. Xu, D.B. Fossan, and J. Gascon, Z. Phys. A **340**, 29 (1991).
[44] G. A. Leander, S. Frauendorf, and F. R. May, *Procedings of the conference on high angular momentum properties of nuclei*, edited by N. R. Johnson, Oak Ridge, Tennesse (Harwood Academic, New York, 1982), p. 281.